

ELECTRONIC AND THERMOELECTRIC PROPERTIES AT THE INTERFACE OF
ORGANIC THERMOELECTRIC MATERIALS

A Dissertation

by

JUI-HUNG HSU

Submitted to the Office of Graduate and Professional Studies of
Texas A&M University
in partial fulfillment of the requirements for the degree of

DOCTOR OF PHILOSOPHY

Chair of Committee,	Choongho Yu
Committee Members,	Lei Fang
	Svetlana Sukhishvili
	Xiaofeng Qian
Head of Department,	Ibrahim Karaman

May 2018

Major Subject: Materials Science and Engineering

Copyright 2018 Jui-Hung Hsu

ABSTRACT

Composites made of poly(3,4-ethylenedioxythiophene):poly(styrenesulfonate) (PEDOT:PSS) and carbon nanotube (CNT) have shown unchanged or even increased thermopower when electrical conductivity was raised by altering the concentration of CNT and/or treating the composites with a polar solvent, dimethyl sulfoxide (DMSO) or an acid, formic acid (FA). In this study, an intermediate CNT concentration showed the highest thermopower and power factor unlike other typical reports with organic composites. The origin of the unusual transport properties was suggested by studying changes in the relative ratio of conducting PEDOT core and insulating PSS, morphology, and carrier concentration and mobility. Our results indicate that the PSS removal by DMSO and FA could alter the carrier transport barrier, and CNT-PEDOT junctions could increase thermopower for composites with a low CNT concentration by avoiding direct contacts between CNTs. For further studying the role of energy barrier at the junctions, organic electrochemical transistor (OECT) was employed as a vehicle to modulate relative energy levels of PEDOT and CNT. By constructing the band diagram at the junction with HOMO, LUMO, and Fermi levels determined by CV, KPFM, and UPS with and without applying gate voltage, the correlation between electrical and thermoelectric properties and the energy barrier height was established. An optimized power factor of $1047 \mu\text{W}/\text{m}\cdot\text{K}^2$ was obtained with a 15 V gate voltage and 0.27 eV energy barrier. The improvement of power factor was attributed to the enhancement of thermopower due to energy filtering effect with minimally affected electrical

conductivity. Further, devices with 1 through 8 CNT-PEDOT junctions were fabricated with barrier height fine-tuned through hydrazine reduction to the optimized condition (0.27 eV). A promising power factor of up to $1299 \mu\text{W}/\text{m}\cdot\text{K}^2$ was obtained with a device with 6 junctions.

DEDICATION

This dissertation is dedicated to my beloved and supportive family, for their endless encouragement, unconditional trust, and true love.

ACKNOWLEDGEMENTS

First, I would like to sincerely thank my supervisor, Dr. Choongho Yu, for his patient guidance, support, advice and inspiration to my research throughout my Ph.D. course. Dr. Yu's enthusiasm and commitment to the research is what I need to carry on in my future career. I also truly appreciate the help and suggestions from my committee members, Dr. Lei Fang, Dr. Svetlana Sukhishvili, and Dr. Xiaofeng Qian.

Also, I appreciate the members of Nano Energy Lab for their friendship and support. I would like to present my deep gratitude to my family, for their numerous supports and sacrifices. Finally, I sincerely thank my fiancée, Bonnie, who always stands by me in joy and sorrow. Words cannot express how grateful I am for the love and trust they have shown me.

CONTRIBUTORS AND FUNDING SOURCES

Contributors

This work was supervised by a dissertation committee consisting of Professor Choongho Yu, Professor Svetlana Sukhishvili, and Professor Xiaofeng Qian of the Department of Materials Science & Engineering and Professor Lei Fang of the Department of Chemistry.

The characterizations depicted in Chapter III were conducted in part by Woongchul Choi of the Department of Materials Science & Engineering and Gang Yang of the Department of Mechanical Engineering and were published in 2017.

All other work conducted for the dissertation was completed by the student independently.

Funding Sources

This work was made possible by the financial support from the U.S. Air Force Office of Scientific Research (Grant No. FA9550-13-1-0085) under the auspices of Dr. Charles Lee.

TABLE OF CONTENTS

	Page
ABSTRACT	ii
DEDICATION	iv
ACKNOWLEDGEMENT	v
CONTRIBUTORS AND FUNDING SOURCES	vi
TABLE OF CONTENTS	vii
LIST OF FIGURES	ix
LIST OF TABLES	xiii
CHAPTER I INTRODUCTION	1
1.1 Background	1
1.2 Objectives and dissertation outline	5
CHAPTER II LITERATURE REVIEW	8
2.1 Strategies for thermoelectric properties improvement	8
2.2 Organic thermoelectric composites – materials and performance	10
2.3 Electronic properties of carbon nanotubes	16
2.4 Energy filtering effect	19
CHAPTER III SOLVENT/ACID TREATED THERMOELECTRIC COMPOSITE MADE OF CARBON NANOTUBES FILLED CONJUGATED POLYMER	23
3.1 Introduction	23
3.2 Experimental	24
3.2.1 Sample preparation	24
3.2.2 Thermopower and electrical conductivity measurements	25
3.2.3 X-ray photoelectron spectroscopy (XPS)	27
3.2.4 Tunneling atomic force microscopy	27
3.2.5 Hall measurements	28
3.2.6 Thermopower of composites	29
3.2.7 PEDOT:PSS/DWCNT-DMSO composites	31
3.2.8 Error analysis for electrical conductivity, thermopower, and the power factor	31

3.3 Results and discussion	33
3.3.1 Microscopic morphology of PEDOT:PSS/CNT composites	33
3.3.2 Thermoelectric properties of PEDOT:PSS/CNT composites	35
3.3.3 Origin of largely increased electrical conductivity after solvent/acid treatment	38
3.3.4 Origin of unchanged thermopower after solvent/acid treatment	43
3.3.5 Origin of maximized thermopower at intermediate CNT concentration .	46
3.4 Conclusions	51
CHAPTER IV ENERGY BARRIER TUNING AT THE INTERFACE OF ORGANIC THERMOELECTRIC MATERIALS FOR THERMOELECTRIC PROPERTIES IMPROVEMENT	52
4.1 Introduction	52
4.2 Experimental	53
4.2.1 Organic electrochemical transistor (OECT) device fabrication	53
4.2.2 Thermopower and electrical conductivity measurements	54
4.2.3 Cyclic voltammetry (CV)	54
4.2.4 Ultraviolet visible near infrared (UV-vis-NIR) spectroscopy and Tauc plot	55
4.2.5 Ultraviolet photoelectron spectroscopy (UPS)	56
4.2.6 Kelvin probe force microscopy (KPFM) measurement	56
4.2.7 Fabricating PEDOT-CNT multi-junction samples by lift-off processes ..	57
4.2.8 Fabricating PEDOT-CNT multi-junction samples by layered processes .	58
4.3 Organic electrochemical transistor (OECT) – design, operation, and analysis .	59
4.4 Results and discussion	64
4.4.1 Thermoelectric properties of PEDOT-CNT junction in OECT	64
4.4.2 Band diagram construction	66
4.4.3 Barrier height analysis	75
4.4.4 PEDOT-CNT multi-junction device fabrication	80
4.5 Conclusions	84
CHAPTER V SUMMARY	85
REFERENCES	88

LIST OF FIGURES

	Page
Figure 1	Electrical conductivity (σ), thermopower (α), thermal conductivity (κ), and figure-of-merit (ZT) as the function of carrier concentration.[1] 3
Figure 2	(n,m) values (chiral vector) and corresponding electronic properties of CNTs. Note that $(n,0)$ CNTs are called zigzag CNTs; (n,n) CNTs are called armchair CNTs.[64] 18
Figure 3	Bandgap as a function of CNT diameters. The filled circles indicate bandgap of zigzag $(n,0)$ tubes with $n = 3k$. The filled diamonds indicate bandgap of chiral (n,m) tubes with $n - m = 3k$. Open circles indicate bandgap of zigzag $(n,0)$ tubes with $n - m \neq 3k$. Open diamonds indicate bandgap of tubes with $n - m \neq 3k$.[65] 19
Figure 4	Energy barrier with proper barrier height at the interface of metallic CNT and p-type polymer can allow high energy charge carriers (hole) to pass while blocking low energy carriers. 20
Figure 5	(a) Transport of charge carriers under a magnetic field (B) in a macroscopically “inhomogeneous” composite with an insulating matrix and conducting inclusions. Due to the large dimension of the inclusion and the insulating matrix, the transport path is limited along the percolated networks of the conducting inclusions, showing non-ideal Hall effects. (b) Transport of charge carriers under a magnetic field in a macroscopically “homogeneous” composite with a conducting matrix and conducting inclusions. The small dimension of the inclusion and the conducting matrix minimally influences the transport path of the charge carrier. For instance, the zigzag-shape black line may indicate non-ideal charge transport, but the overall path (red line) is similar to that from typical Hall effects. 29
Figure 6	Composites consist of conducting gold particles and an insulating polymer matrix. The gold particles form one (a), two (b), three (c), or some percolated chains (d). 30
Figure 7	SEM images of cold-fractured cross sections of pristine PEDOT:PSS (a) and PEDOT:PSS/CNT composites containing 2-wt% CNT (b), 6-wt% CNT (c), and 20-wt% CNT (d). The inset shows a portion contains aggregated CNTs. 34

Figure 8	TUNA current mapping of PEDOT:PSS/CNT composites whose CNT concentration is 2.2 wt% (a), 6.7 wt% (b), and 20 wt% (c). Brighter lines indicate more conducting CNTs and the darker background corresponds to PEDOT:PSS whose electrical conductivity is lower than that of CNT.....	35
Figure 9	Electrical conductivity (a), thermopower (b), and power factor (c) of PEDOT:PSS/CNT composites when the CNT concentration was varied from 0 to 20 wt% before and after DMSO/FA treatments.	37
Figure 10	(a) XPS survey scan of PEDOT:PSS before and after the DMSO or FA treatment. S 2p XPS spectra of pristine PEDOT:PSS (b), PEDOT:PSS treated by DMSO (c), and PEDOT:PSS treated by FA (d). The fitted peaks and the component peaks for sulfur in PEDOT (165 eV and 163.8 eV) and PSS (167.8 eV and 168.9 eV) are also shown.	40
Figure 11	The AFM images of pristine PEDOT:PSS (a) and PEDOT:PSS treated by DMSO (b) and FA (c), and their root-mean-square roughnesses are 1.49, 1.11, and 0.95 nm, respectively. The edge length of the images is 750 nm. The estimated morphology of PEDOT:PSS corresponding to 'a', 'b', and 'c' is illustrated in (d), (e), and (f), respectively. The dashed line indicates hole transport across PEDOT:PSS grains. The smaller grains in 'e' have more percolated pathways compared to 'f'. The AFM images of PEDOT:PSS with 6.67-wt% CNT prior to any treatment (g) and after the DMSO (h) and FA (i) treatment.	42
Figure 12	Conceptual illustration of PEDOT:PSS/CNT composites when the CNT concentration is low (a) and high (b). Note that the illustration is not to scale. With a low CNT concentration, carrier transport occurs mainly through CNT-PEDOT:PSS-CNT junctions whereas carriers travel directly through a CNT to another CNT. Energy band diagrams corresponding to 'a' and 'b' are shown respectively in (c) and (d), suggesting the presence of an energy barrier for the case of 'a'.	48
Figure 13	Electrical conductivity (a), thermopower (b), and power factor (c) of DMSO-treated PEDOT:PSS/DWCNT composites with DWCNT concentrations from 0 to 20 wt%.	50
Figure 14	Fabrication steps of PEDOT-CNT multi-junction samples by lift-off processes. One junction sample is shown as an example.	58
Figure 15	Fabrication steps of PEDOT-CNT multi-junction samples by layered processes.	59

Figure 16 The design of organic electrochemical transistor (OECT) device in this study.	60
Figure 17 Energy band diagrams showing the barrier height between CNT and PEDOT at different scenarios. For a contact between metallic CNT and PEDOT, given that work function of CNT is larger than that of PEDOT, the barrier height can be expressed as $E_{gp} - \phi_p + \chi_p$. For a contact between metallic CNT and PEDOT, given that work function of CNT is larger than that of PEDOT, the barrier height can be expressed as $E_{gp} - E_{gCNT} + \phi_{CNT} - \phi_p + \chi_p - \chi_{CNT}$	63
Figure 18 Electrical conductivity, thermopower, and power factor of CNT-PEDOT-CNT junction when SWCNT ((a), (b)), DWCNT ((c), (d)), and MWCNT ((e), (f)) was used for the CNT region.	66
Figure 19 (a) CV curve of SWCNT. The red crosses show the onset potential of oxidation and reduction peaks. (b) Tauc plot: $(\alpha E_{ph})^2$ as a function of E_{ph} calculated from UV-vis-NIR absorption spectrum of SWCNT. The optical bandgap of SWCNT is determined by the extrapolation line to be 0.53 eV. (c) Cut-off and (d) onset region of the UPS spectra of SWCNT. The Fermi level and HOMO can be found to be 5.02 eV and 5.00 eV, respectively. ...	68
Figure 20 CV curve of PEDOT (a) and DWCNT (b). For PEDOT, HOMO and LUMO are determined to be 4.83 eV and 3.98 eV, respectively. For DWCNT, HOMO and LUMO are determined to be 4.89 eV and 4.51 eV, respectively.	69
Figure 21 Tauc plot of DWCNT. The optical bandgap of DWCNT is determined by the extrapolation line to be 0.48 eV.	69
Figure 22 Cut-off and onset region of the UPS spectra of PEDOT ((a), (b)), DWCNT ((c), (d)), and MWCNT ((e), (f)). The Fermi level and HOMO of PEDOT are 4.67 eV and 4.81 eV, respectively. The Fermi level and HOMO of DWCNT are 4.67 eV and 4.81 eV, respectively. The Fermi level and HOMO of MWCNT are both 4.78 eV.	70
Figure 23 (a) CPD profile of PEDOT, SWCNT, DWCNT, and MWCNT obtained from KPFM. (b) CPD profile of PEDOT as gate voltages of 0, 5, 10, 15, and 20 V were applied.	72
Figure 24 HOMO, LUMO, and Fermi levels of PEDOT, SWCNT, DWCNT, and MWCNT determined by CV, UPS, and KPDM. The Fermi levels of PEDOT measured as gate voltage of 0, 5, 10, 15, and 20 V were applied are also shown.	74

Figure 25 Band diagram of CNT-PEDOT-CNT junction made of SWCNT (a), DWCNT (b), and MWCNT (c) when no gate voltage (left) and gate voltage of 20 V are applied. Increase of barrier height for charge carrier can be seen as gate voltage is applied. 76

Figure 26 Schematic diagram showing an OECT device bridged between hot side and cold side. ΔT_{CNT} (the temperature difference across CNT region) and $\Delta T_{polymer}$ (the temperature difference across the PEDOT region) are indicated. 77

Figure 27 (a) Electrical conductivity, thermopower and (b) power factor of intrinsic PEDOT, SWCNT, DWCNT, and MWCNT. Gate voltage dependent thermoelectric properties of PEDOT are also shown in (c) and (d). 78

Figure 28 The relative contribution of thermopower from intrinsic property change and energy barrier filtering for devices made of SWCNT (a), DWCNT (b), and MWCNT (c). The percentages of thermopower improvement ($S_{total}/S_{intrinsic}$) due to energy filtering for devices made of different kinds of CNTs as a function of gate voltage are shown in (d). 79

Figure 29 (a) Electrical conductivity and thermopower and (b) power factor of devices with 1 to 5 PEDOT-CNT junctions fabricated by lift-off method. . 81

Figure 30 (a) Electrical conductivity and thermopower and (b) power factor of devices with 1 to 10 PEDOT-CNT junctions fabricated by layered method. 83

LIST OF TABLES

	Page
Table 1 Highest reported thermoelectric properties of conjugated polymers.	13
Table 2 Thermoelectric performance of organic thermoelectric composites.....	16
Table 3 Relative amount of PEDOT and PSS estimated by XPS. A_{PEDOT} and A_{PSS} are respectively the sum of the area of component peaks from PEDOT and PSS. ...	40
Table 4 Hall mobility and carrier concentration of the PEDOT:PSS composites with 6.67-wt% CNT and without CNT before and after the DMSO or FA treatment.	43
Table 5 Electrical bandgap (obtained from CV), optical bandgap (obtained from UV-vis), and theoretical bandgap of SWCNT and DWCNT.	71

CHAPTER I

INTRODUCTION

1.1 Background

Developing and discovering new sources of energy have become one of the major focuses of the scientific community in recent years, especially combustion of fossil fuels, the current major energy source, suffers from the problems of limited supply and air pollution. Thermoelectric generator (TEG) is an alternative energy source that utilizes Seebeck effect that converts temperature difference directly into electricity. TEG can also be used as heat pumps based on Peltier effect, a reversed effect of Seebeck effect, when power is externally supplied. TEG devices contain no moving parts and liquid/gas media, and are thus quiet, low maintenance, and environmental friendly. Moreover, low-grade heat, which is otherwise wasted, can be utilized by TEG devices to generate electricity. Thus, thermoelectric devices gather much attention and interest from the industry and academia. To name a few of the applications of thermoelectric devices, TEG can be used to recycle waste heat from automobile engine and industrial processes, and even to power small portable devices or sensors with low temperature energy sources like body temperature.

The performance of thermoelectric energy generation is often described by a dimensionless figure-of-merit called $ZT = S^2\sigma T/\kappa$, where S , σ , κ , T stand for thermopower (or Seebeck coefficient), electrical conductivity, thermal conductivity, and absolute temperature, respectively. When the variation of thermal conductivity is not a major

concern, the thermoelectric performance of materials can also be estimated by power factor (PF), which is given by $PF = S^2\sigma$. ZT is related to energy conversion efficiency, which is the output electrical energy divided by the input thermal energy, by the following equation:

$$\eta = \frac{T_H - T_C}{T_H} \left[\frac{\sqrt{1 + ZT_m} - 1}{\sqrt{1 + ZT_m} + T_C / T_H} \right]$$

where η is the energy conversion efficiency, T_H and T_C are hot side and cold side temperatures, respectively, and ZT_m is the figure of merit at the medium temperature between T_H and T_C . Note that the term $(T_H - T_C)/T_H$ is the Carnot efficiency.

ZT improvement is fundamentally important for enhancing energy conversion efficiency. We can see from the expression $ZT = S^2\sigma T/\kappa$, large ZT requires high thermopower to create high thermoelectric voltage, high electrical conductivity to efficiently transport energy through electrical charges, and low thermal conductivity to maintain large temperature difference. However, thermopower, electrical conductivity, and thermal conductivity are inter-correlated. It is challenging to optimize one parameter without affecting the others, this being the major hurdle for thermoelectric performance improvement. For example, according to Wiedemann-Franz law, electrical conductivity and thermal conductivity are inter-related with the equation $\sigma T/\kappa = (3/\pi)^2(q/k_B)^2$, where k_B is Boltzmann constant. It can be seen that improving electrical conductivity inevitably raises thermal conductivity, due to the fact that electrons conduct both electricity and heat. Also, according to the equation $\sigma = ne\mu$, electrical conductivity is proportional to both carrier concentration (n) and carrier mobility (μ). With Mott relation, $S =$

$\pi^2 k_B^2 m^* T / (3\pi^2)^{2/3} \hbar |e| n^{2/3}$, where m^* is the effective mass of an electron, \hbar is the Planck constant, thermopower is inversely related to carrier concentration. Thus raising electrical conductivity by increasing carrier concentration could diminish thermopower. The relationship between thermopower, electrical conductivity, and thermal conductivity can be manifested in Figure 1.[1]

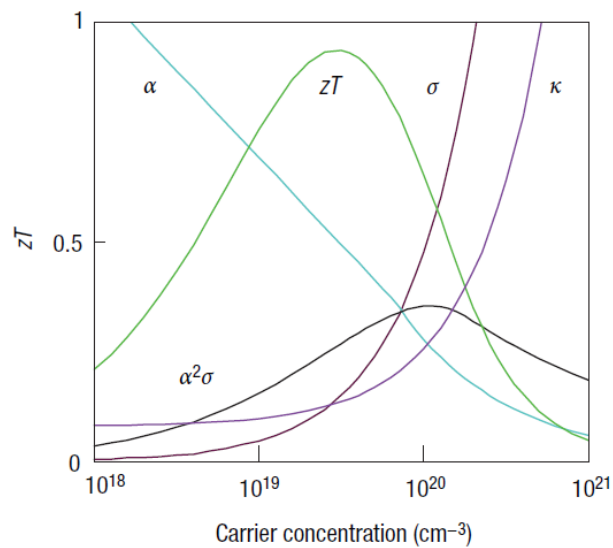


Figure 1. Electrical conductivity (σ), thermopower (α), thermal conductivity (κ), and figure-of-merit (ZT) as the function of carrier concentration.[1] (reprinted from [1] with permission)

From the materials' perspective, we would like to choose materials or combination of materials that are most suitable for thermoelectric applications. Generally speaking, insulators or intrinsic semiconductors are too resistive to give large enough electrical conductivity, and metals suffer from their high thermal conductivity and typically low thermopower ($\sim 10 \mu\text{V/K}$). Therefore, appropriate candidates are doped semiconductors. In fact, inorganic semiconducting materials (e.g. PbTe, ZnSb, SnSe, etc.) [2-13] have been the major focuses of thermoelectric material research. With carrier concentration adjusted to be between 10^{19} cm^{-3} to 10^{20} cm^{-3} and the efforts to reduce thermal conductivity without sacrificing electrical conductivity by nano-engineering, ZT values above unity are generally achieved for inorganic thermoelectric materials.[14] However, inorganic thermoelectric materials suffer from several shortcomings. The fabrication of inorganic thermoelectric materials requires both time and energy-consuming fabrication processes, such as high-energy ball milling and hot pressing. Also, their common component elements such as Pb, Sb, Te, etc., are toxic and of limited supply. Furthermore, the materials are typically heavy and brittle, and thus are not suitable for portable or wearable device applications. On the contrary, the counterpart of organic semiconductors such as conjugated polymers and small molecules have the advantages of flexible, light weight, and are solution-processable (which infers low cost). Additional benefits of organic materials include their low thermal conductivity (less than 1 W/m-k) and high mobility possibly rivaling the mobility of polycrystalline silicon.[15] Also, benefited from the knowledge accumulated from the development of materials along with the research of organic field effect transistors

(OFETs), organic light-emitting diodes (OLEDs), and organic photovoltaics (OPVs), physical and chemical properties of organic materials are highly tunable through rationally designed synthetic or fabrication routes and doping treatments.[16] These advantages render organic materials promising for thermoelectric applications, especially at low temperatures. Recent efforts have shown promising results of energy harvesting/conversion based on organic thermoelectric materials.[17-25] In spite of the aforementioned benefits, their low carrier mobility and mediocre thermopower are the two major factors hindering them from further property improvement.

1.2 Objectives and dissertation outline

In the first part of this dissertation, thermoelectric composites based on conjugated polymer and carbon nanotubes were investigated. The combined strategies of hybridization and solvent treatment were employed for developing high performance thermoelectric composites. I aim to clarify the interaction between the component materials of the composite, as well as to reveal the underlying relationship between composition, morphology and electrical and thermoelectric behaviors. The ultimate goal is to suggest viable strategies for further properties improvement.

In the second part of the dissertation, I focus on the investigation of the effect of energy barrier at the interface of materials on thermoelectric performance. Energy barrier in a composite system was found to be of crucial importance to thermoelectric properties, as revealed by the first part of this research. I aim to further study the effect of energy barrier (or energy filtering) on thermoelectric performance in terms of barrier

height and the number of barriers utilizing organic electrochemical transistor (OECT) as a vehicle. The final objective is to enhance the performance of thermoelectric devices by interfacial energy barrier engineering.

The outline of the dissertation is described as the following. In Chapter II, commonly employed strategies for improving thermoelectric properties of organic materials are reviewed. Then representative studies of thermoelectric composites in terms of materials and performance are highlighted and summarized, followed by a brief introduction to the electronic properties of carbon nanotubes, which is the filler material employed in this research. In the end of this chapter, theoretical and experimental researches related to energy filtering effect of both organic and inorganic materials are reviewed to shed light on the approaches and strategies to adopt in the current study.

Chapter III investigates thermoelectric composites based on conjugated polymer and carbon nanotubes. After studying the microscopic morphology of the composites, the electrical and thermoelectric behaviors of the composite are presented and discussed. Then three intriguing behaviors exhibited by the composite are identified and further explored, including the origin of largely increased electrical conductivity but unchanged thermopower after solvent/acid treatment, as well as the maximized thermopower at intermediate CNT concentration. Concluding remarks are made to suggest the directions for making high performance composites.

In Chapter IV, organic electrochemical transistor (OECT) was employed to study the effect of energy barriers at the PEDOT-CNT junctions. Design, operation, and analysis methods of the OECT are described first. Subsequently, thermoelectric

properties of PEDOT-CNT junction in OECT with different kinds of CNTs and with varied gate voltages are presented. Then band diagrams are constructed based on measurement of energy levels to quantitatively estimate the barrier heights at PEDOT-CNT junctions. The improvement of thermoelectric properties originated from energy barrier is discussed. Finally, with suggested optimized energy barrier condition, multi-junction devices are fabricated and analyzed to best exploit the effect of energy filtering for thermoelectric properties improvement.

Lastly, Chapter V provides summary of this dissertation and directions for future research.

CHAPTER II

LITERATURE REVIEW

2.1 Strategies for thermoelectric properties improvement

There are a number of strategies researchers adopt for improving thermoelectric performance of organic thermoelectric materials. Benefited from the widely-tunable nature of electronic structure of organic semiconductors, one of the widely employed approaches is to fine tune the carrier concentration or doping level of these materials. As mentioned previously, with inter-correlated thermopower, electrical, and thermal conductivity, all of which are dictated by carrier concentration, optimizing carrier concentration or doping level is an effective way for enhancing thermoelectric properties. For example, Crispin *et al.* optimized thermoelectric properties of PEDOT:tos by treating it with a reducing agent, tetrakis(dimethylamino)ethylene (TDAE) to change the doping level of PEDOT:tos. UV-vis spectra and XPS were used to verify and quantify the change of doping level. The power factor was optimized as the doping level was around 22 %.[17] The same group employed a different route for thermoelectric property optimization through electrochemical transistor architecture. Oxidation level of the PEDOT:PSS “channel” in the transistor was altered by applying gate voltage through a “gate” in parallel with the “channel”.[26] The same strategy was applied to a different kind of conjugated polymer, poly(3-hexylthiophene) (P3HT). For example, P3HT film was doped with NOPF_6 and $\text{Fe}(\text{TFSI})_3$ stepwise so as to change the doping level from 0 % to 35 %. The power factor was improved by three orders of

magnitude with a doping level of 25 %.[27] Though many papers have reported the optimization of doping level for thermoelectric performance improvement, there is no consistent definition of doping level. Also, the optimized doping level varies from one work to another.

On the other hand, microscopic morphology control is an alternative way to effectively enhancing the performance of organic thermoelectric materials. Morphological factors, such as crystallinity of polymers, crystal orientation, and chain conformation determine transport mechanisms of charge carriers (e.g. hopping, diffusion, etc.). Charge carrier transport, in turn, influences thermopower, electrical conductivity, and thermal conductivity in different ways. For example, charge carrier mobility (which affects electrical conductivity according to the formula $\sigma = ne\mu$) can be largely increased by increasing crystallinity according to previous study of field effect mobility of polymers.[28, 29] Also, material defects such as grain boundary could scatter phonons and impede heat transport while allowing charge carriers to transport through, improving thermoelectric performance.[30] Morphology of organic thermoelectric materials can be controlled through controlling synthesis processes and post treatments. For example, D. B. Zhu *et al.* synthesized β -Naphthalene sulfonic acid doped polyaniline (PANI) nanotubes together with PANI samples without specific nanostructure for comparison.[31] They found doubled electrical conductivity and 7-time higher thermopower for tubular-structured samples. As a result, the ZT value of the tube-like PANI was two orders of magnitude higher than its counterpart. Similarly, Taggart *et al.* prepared PEDOT nanowires using the lithographically patterned nanowire electro-

deposition process.[32] The power factor of the PEDOT nanowire was improved compared to PEDOT films without specific orientation owing to enhanced crystallinity and charge carrier mobility. Also, Chen *et al.* fabricated highly anisotropic P3HT films with enhanced thermoelectric performance via small molecule epitaxy of trichlorobenzene (TCB).[33] With enhanced carrier mobility and almost non-affected thermopower via the orientation of polymer chains, a high power factor of $62.4 \mu\text{W}/\text{mK}^2$ was reported. Lastly, post treatments such as solvent treatment or annealing can also alter film morphology as characterized by AFM and TEM.[34] Huge improvement of thermoelectric properties of PEDOT:PSS treated by ethylene glycol (ZT up to 0.42) was reported.[35]

2.2 Organic thermoelectric composites – materials and performance

Having discussed the ways for thermoelectric properties improvement for single component materials, in the materials design point of view, making composites comprise of multiple components of materials formed by hybridization of organic matrix with organic/inorganic fillers has been another popular approach. Essentially, composite fabrication is an easy and viable way for modifying the properties of materials (including carrier concentration, carrier mobility, and microscopic morphology, the properties we already discussed and proven to be crucial to thermoelectric performance) by changing the ratio and method for hybridization. Also, thermoelectric performance could benefit from the interaction of component materials, so a composite could have properties not achievable from its component materials. In addition, the massive interface between

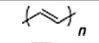
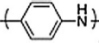
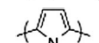
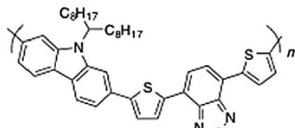
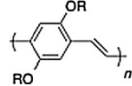
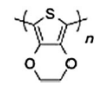
component materials formed in the nanocomposite could play a key role for thermoelectric properties improvement. For example, the interface could serve as phonon scattering sites that reduce thermal conductivity.[36-38] Also, the energy barrier at the interface originated from the Fermi level mismatch of the component materials could have energy filtering effect that potentially raises thermopower, as is one of the major focuses of this dissertation. As a result, thermoelectric composite fabrication provides a route for combining the benefits of the component materials to achieve performance better than each of the components.

There could be huge variation of ways that how a thermoelectric composite can be formed. The polymer matrix could be insulating or conductive. The filler particles could be organic, inorganic, and could be variable in size and shapes (i.e. spheres, rods, tubes, wires, and platelets).[39] Composites can be prepared by polymerization of monomer mixed with filler nanoparticles, reduction of precursors to form filler particles in the presence of polymer matrix, or simply forming the solution mixture of the filler and the polymer.

For the polymer materials in the composite, a number of conjugated polymers have been investigated for thermoelectric applications, including poly(phenylene vinylenes) (PPV),[40] polythiophenes,[27] polycarbazoles,[41] polypyrrole (PPy),[42] polyacetylene (PA),[43] and polyaniline (PANI).[44] The highest reported thermoelectric properties of conjugated polymers are summarized in Table 1.[39] Among all the conjugated polymers, poly(3,4-ethylenedioxythiophene) (PEDOT) has been one of the most popular organic thermoelectric materials. Its electrical conductivity

and thermopower are widely tunable using reducing agents[45-47], electrochemical routes,[26] or morphology control. Morphology control with organic solvents such as ethylene glycol (EG),[48] dimethyl sulfoxide (DMSO),[21] and methanol (MeOH)[49] have been reported. The progress of thermoelectric properties improvement of PEDOT-based thermoelectric materials has been significant since 2010. In 2011, Crispin *et al.* demonstrated an impressive power factor of $324 \mu\text{W}/\text{m}\cdot\text{K}^2$ and ZT of 0.25 with PEDOT:tos de-doped with tetrakis(dimethylamino)-ethylene (TDAE).[45] The high power factor was originated from the high thermopower ($>200 \mu\text{V}/\text{K}$). Kim *et al.* employed electrochemical routes to control the doping level of PEDOT:tos films, achieving a power factor of $862.9 \mu\text{W}/\text{m}\cdot\text{K}^2$ for as synthesized film and $1290 \mu\text{W}/\text{m}\cdot\text{K}^2$ for slightly de-doped film.[50] Mossonnet *et al.* investigated the relationship between the redox potential of the reducing agents and the thermopower of PEDOT:PSS film, proposing that redox potential could be utilized for carrier density control.[51]

Table 1. Highest reported thermoelectric properties of conjugated polymers.[39]
(reprinted from [39] with permission)

Material	Structure	Dopant	σ [S cm ⁻¹]	α [μ V K ⁻¹]	PF [W m ⁻¹ K ⁻²]
PA		I ₂	44 250	14	2.7 × 10 ⁻⁴
PANI		CSA ⁻	160	5	4 × 10 ⁻⁷
PPy		PF ₆ ⁻	340	10.5	2 × 10 ⁻⁶
Polycarbazole derivatives		FeCl ₃	160	34	1.9 × 10 ⁻⁵
PPV derivatives		I ₂	349	47	7.8 × 10 ⁻⁵
PEDOT:PSS		DMSO/EG	890	74	4.7 × 10 ⁻⁴

Abbreviations: PA = polyacetylene, PANI = polyaniline, PPy = polypyrrole, PPV = poly(phenylene vinylene), PEDOT = poly(3,4-ethylenedioxythiophene), PSS = polystyrene sulfonate, CSA = camphor sulfonate, DMSO = dimethyl sulfoxide, EG = ethylene glycol.

On the other hand, to further improve TE properties of conjugated polymers, nanoscale fillers including carbon nanotube (CNT),[20, 21, 52, 53] graphene,[22] Bi₂Te₃ particles,[54] gold nanoparticles,[55] and Te nanorods[56] have been hybridized to synthesize nanocomposites. Among them, CNTs have promising properties such as their outstanding electrical conductivity and mechanical strength. Though they have large thermal conductivities ($k > 1000$ W/m-K for SWCNTs),[57] much lower values ($k < 35$ W/m-K) were obtained when CNTs are in forms of bundles, ropes, or mats.[58] It has been reported recently that via proper sorting of CNTs with desirable chirality distribution and carrier concentration, a promising power factor of $340 \mu\text{W}/\text{m-K}^2$ can be achieved.[57] A brief review of electrical properties of CNTs will be provided in section 2.3.

Here we focus on the review of representative works based on the thermoelectric composites formed by conjugated polymers with carbon-based materials, especially CNTs. The composites are typically highly conductive, have good mechanical strength, and light weight. Their high thermal conductivity is the major hurdle to achieve high ZT. Carbon based materials could be planar (graphene), spherical (fullerenes), or tubular (CNTs) and they interact with conjugated polymers with different ways. The π - π interaction between carbon-based materials and conjugated polymer can help to overcome the strong van der Waals interactions between carbon-based materials to improve dispersion and can induce morphology and conformation change of polymer chains. Abad *et al.* synthesized a composite made of PANI-HCl and graphene by grinding and cold compression molding.[59] A thermopower of 34 $\mu\text{V/K}$ and power factor of 14 $\mu\text{W/m-K}^2$ were obtained. Zhao *et al.* polymerize aniline in the presence of graphene oxide (GO) platelet to form a composite with strong PANI-platelet interaction. The GO was then reduced into graphene to regain conductivity. However, the ZT obtained was not good (4.86×10^{-4}) due to low electrical conductivity.[60] Grunlan *et al.* utilized layer-by-layer assembly method to fabricate a composite made of alternatively deposited PANI, graphene, and double-wall CNTs. The thin film with 40 quadlayers showed electrical conductivity of 1.08×10^5 S/m, Seebeck coefficient of 130 $\mu\text{V/K}$, and a decent power factor of 1825 $\mu\text{W/m-K}^2$.[22] Yu *et al.* developed composites made of single-wall CNT, PEDOT:PSS, and/or polyvinyl acetate with thermopowers weakly correlated with electrical conductivity. Large power factor of up to 160 $\mu\text{W/m-K}^2$ can be obtained at room temperature.[61, 62] The same group reported thermally driven large

n-type thermoelectric voltage response from hybrids of CNT and PEDOT treated with TDAE.[45] It was claimed that TDAE reduction reduced carrier concentration and led to improved thermopower, while the partially percolated CNT network maintained moderate to high electrical conductivity. A high power factor up to $\sim 1050 \mu\text{W}/\text{m}\cdot\text{K}^2$ was reported.

Thermoelectric performance of composites made of conjugated and insulating polymers hybridized with organic, inorganic, and carbon-based particle additives are summarized in Table 2 for comparison.[39]

Table 2. Thermoelectric performance of organic thermoelectric composites.[39]
(reprinted from [39] with permission)

Matrix	Filler	Filler form	Loading [wt%]	σ [S cm^{-1}]	κ [$\text{W m}^{-1} \text{K}^{-1}$]	α [$\mu\text{V K}^{-1}$]	PF [$\text{W m}^{-1} \text{K}^{-2}$]	ZT
Conductive polymers with polymer and small-molecule additives								
PS	PANI-HCl	blend	0.2	0.046	–	8	6.4×10^{-6}	–
PMMA	PANI-CSA	blend	0.091	10^{-3}	–	8	–	–
P3HT/P3HTT	F ₄ TCNQ	blend	1.2	2×10^{-4}	–	450	1.2×10^{-9}	1.4×10^{-5}
P(NDIOD)-T2	dihydrobenzimidazoles	blend	9	0.004	–	–850	–	–
Conductive polymer matrices with particle additives								
PEDOT:PSS	PbTe	spherical	30	0.003	–	2500	1.45×10^{-6}	–
PEDOT:PSS	Te	nanowire	–	19	0.22	163	7×10^{-5}	0.1
PANI-HCl	Bi ₂ Te ₃	nanowire	30	11.6	0.11	40	2.0×10^{-4}	0.004
PEDOT:PSS	Bi _{0.5} Sb _{1.5} Te ₅	platelet	4.1	1295	–	16	3.2×10^{-5}	–
PANI-HCl	MoS ₂	platelet	85	0.8	–	8	–	–
PPy	MoS ₂	platelet	85	0.8	–	82	–	–
P3OT	Ag	spherical	6	–	–	1283	–	–
PEDOT:PSS	Au	spherical	0.01	241	–	27	1.8×10^{-5}	0.016
PEDOT:PSS	SWCNT	nanotube	35	400	–	23	2.4×10^{-5}	0.02
PEDOT:PSS	SWCNT	nanotube	85	4000	–	16	1.02×10^{-4}	0.03
PANI-MeSO ₃ H	SWCNT	nanotube	6.6	530	–	33	0.6×10^{-6}	–
PANI-HCl	MWCNT	nanotube	1	14	0.27	80	–	0.01
PANI-HCl	graphene	platelet	50	123	–	34	1.4×10^{-5}	–
PANI-HCl	graphene oxide	platelet	10	7.5	0.41	28	6.01×10^{-7}	4.86×10^{-4}
Insulating polymer matrices with particle additives								
PEO	MoS ₂	platelet	72 [mol%]	0.1	–	1.5	–	–
PVOAc	SWCNT	nanotube	20	48	0.34	40	–	0.006
PVOAc/ <i>meso</i> -tetra-(4-carboxyphenyl)-porphine)	MWCNT	nanotube	12	71.1	–	78	10^{-6}	–
PVOAc/sodium deoxycholate	MWCNT	nanotube	12	1.28	–	71	10^{-6}	–
PEI/sodium dodecyl benzenesulfonate	CNT	nanotube	20	8.4	–	100	8.4×10^{-6}	–
PVDF	few-layer graphene	platelet	80	170	–	17	5.2×10^{-7}	–

2.3 Electronic properties of carbon nanotubes

A CNT can be regarded as a cylinder generated by rolling a piece of graphene to form a seamless structure. The circumference of CNT can be expressed by the chiral vector, C , which connects two crystallographically identical sites of 2-D graphene sheet. $C = na_1 + ma_2$, where a_1 and a_2 are primitive lattice vectors of the hexagonal graphene sheet. Thus, any CNT can be described by an integer pair of (n,m) , which determines electronic properties of CNTs. It has been shown that a CNT is metallic (with no

bandgap) when n equals to m ; a CNT has a small bandgap when $n - m$ or $m - n$ is a multiple of 3; a CNT is semiconducting for all other cases.[63] Figure 2 shows chiral vectors and corresponding electronic properties of CNTs.[64] Also, there is a relation between CNT diameter and bandgap, as formulated by $E_{gap} = (4\hbar v_F/3d_{CNT})$, where E_{gap} is the bandgap, d_{CNT} the diameter of CNT, v_F the Fermi velocity and is equal to 8×10^7 m/s. From this relation, bandgap of CNT is inversely proportional to its diameter. This relation has been experimentally proven, as depicted in Figure 3.[65] Accordingly, CNTs with small diameters (single-wall CNT, double-wall CNT) have larger bandgap and are more semiconducting; CNTs with larger diameters (multi-wall CNT) have smaller bandgap and are more metallic.

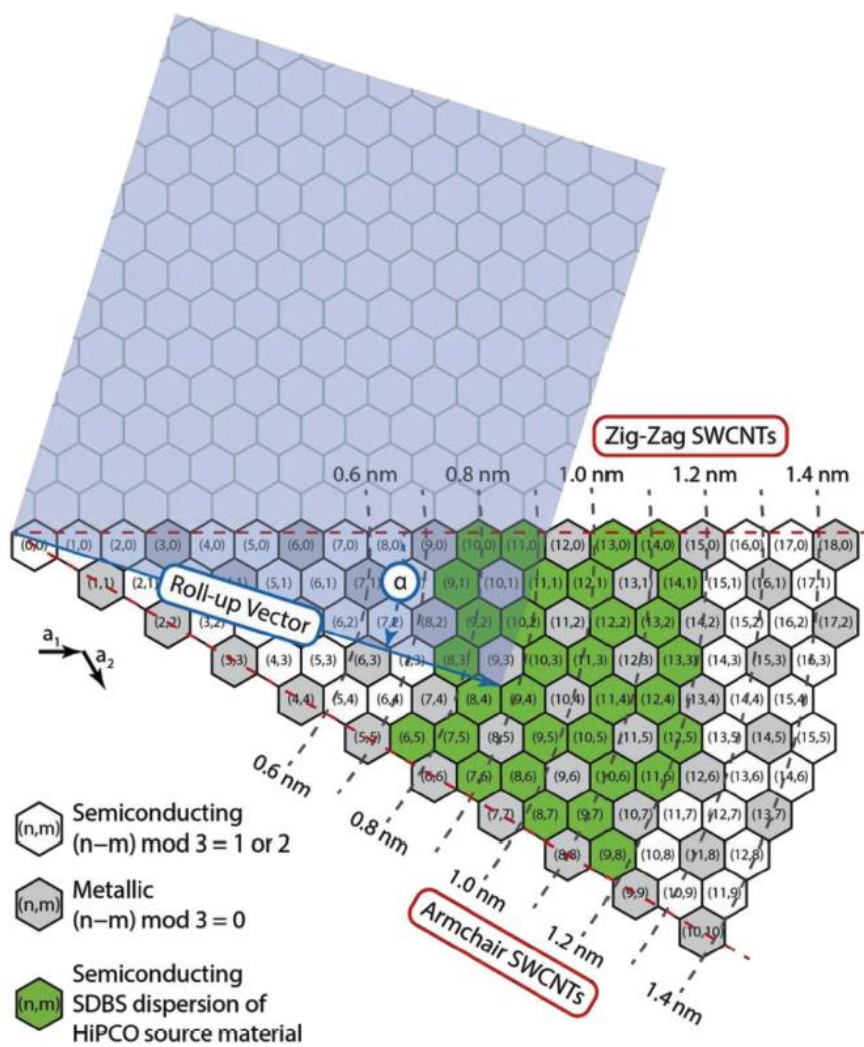


Figure 2. (n,m) values (chiral vector) and corresponding electronic properties of CNTs. Note that (n,0) CNTs are called zigzag CNTs; (n,n) CNTs are called armchair CNTs.[64] (reprinted from [64] with permission)

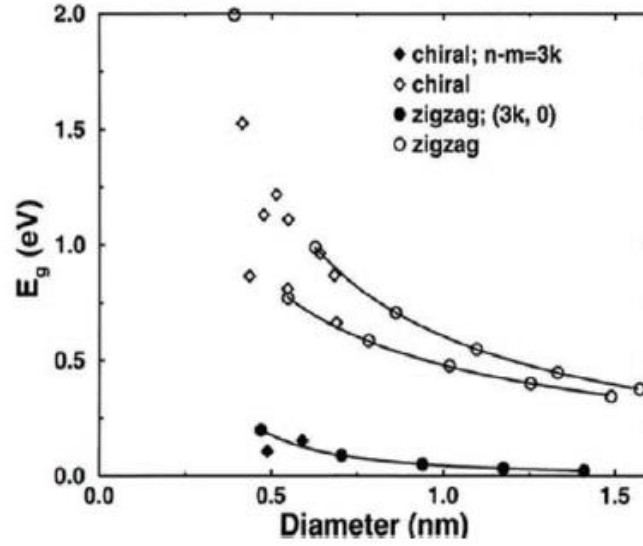


Figure 3. Bandgap as a function of CNT diameters. The filled circles indicate bandgap of zigzag $(n,0)$ tubes with $n = 3k$. The filled diamonds indicate bandgap of chiral (n,m) tubes with $n - m = 3k$. Open circles indicate bandgap of zigzag $(n,0)$ tubes with $n - m \neq 3k$. Open diamonds indicate bandgap of tubes with $n - m \neq 3k$. [65] (reprinted from [65] with permission)

2.4 Energy filtering effect

The concept of energy filtering can be understood with the following equation:

$$S \approx \frac{1}{eT} \langle E - E_f \rangle$$

where e is the electrical charge, T is absolute temperature, E is the energy of charge carriers, E_f is Fermi level, and $\langle E - E_f \rangle$ denotes the average energy difference between charge carriers and Fermi level. Since thermopower is proportional to the energy difference between charge carriers and Fermi level, if energy barriers with appropriate barrier height is introduced into a material system, low energy charge carriers can be filtered out while allowing high energy carriers to transport through. Thus $\langle E - E_f \rangle$ is enlarged and thermopower could be improved. From another point of view,

thermopower is determined by the average entropy transported per charge carrier. Therefore, if charge carriers with greater entropy contribute more to electrical conduction, thermopower can be elevated. Thus, again, filtering out low energy charge carrier is beneficial to thermopower enhancement. With energy filtering, if the increase of thermopower can compensate the decrease of electrical conductivity (because less carriers participate in conduction), power factor can be improved. An exemplified band diagram at metallic CNT and p-type polymer interface is shown in Figure 4 illustrating how a barrier can filter out low energy carrier while allowing high energy carrier to pass.

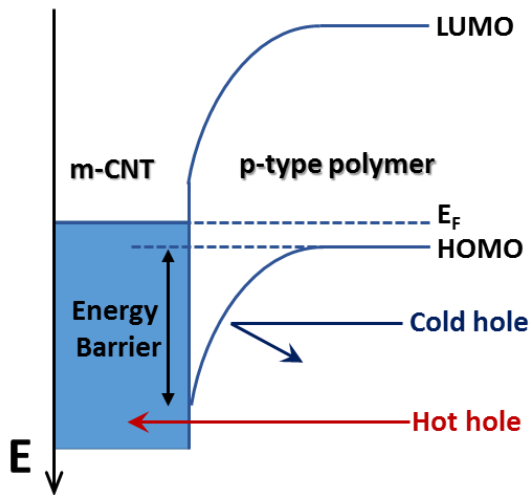


Figure 4. Energy barrier with proper barrier height at the interface of metallic CNT and p-type polymer can allow high energy charge carriers (hole) to pass while blocking low energy carriers.

Studies about energy filtering have been mainly based on inorganic materials. Experimental and theoretical results have shown that energy filtering is an effective route for increasing power factor. Experimentally, energy filtering is accomplished by introducing nanoparticles into a matrix material or creating superlattices (periodic

layered structure of two or more materials) to introduce huge amount of interface between materials. For example, Shakouri *et al.* reported that a InGaAs/InGaAlAs superlattice showed enhanced power factor due to energy filtering effect.[66] Also, improvement of thermopower owing to energy filtering in bulk nanostructured PbTe based materials was reported by Morelli *et al.*[67, 68] In the work of Stucky *et al.*, $\text{Ag}_x\text{Te}_y\text{-Sb}_2\text{Te}_3$ hetero-structured film was reported to have over 50% enhanced thermoelectric power factor because the created interfacial barrier can scatter cold carriers stronger than hot carriers.[69]

In the field of organic thermoelectric materials, some research groups have made organic thermoelectric composites with enhanced power factor claimed to be due to energy filtering effect. For instance, Meng *et al.* fabricated CNT/PANI nanocomposites and found that the power factor was several times larger than that of the individual components. They attributed this behavior to the size-dependent energy filtering effect originated from nanostructured PANI wrapping around CNT networks.[70] Wang *et al.* made composites based on functionalized graphene with fullerene and PEDOT:PSS. The created interface between component materials was considered to potentially introduce energy filtering effect that led to 4-fold improvement in the thermopower.[71] However, these works are deficient of experimental measurement of materials energetics and the measured thermoelectric properties of their composites were not compared to pristine component materials. Thus, it is hard to identify the role of energy filtering. On the other hand, some groups attempted to construct band diagram at material interfaces by measuring energy levels in the system, trying to quantitatively reveal the effect of energy

barrier height on the thermoelectric properties. Yu *et al.* employed a “doping/de-doping” approach to maintain proper barrier heights at CNT-PANI junctions while improving overall conductivity of the composite.[72] Barrier heights at CNT-PANI junction were determined by energy levels measurement and correlated to thermopower based on theoretical calculation. Great power factor improvement was obtained due to large enhancement of electrical conductivity (~700 %) without significantly sacrificing thermopower (90 % remained). Kim *et al.* made composite films comprised of reduced graphene oxide (rGO), PEDOT:PSS and Te nanowires.[73] The power factor obtained from the ternary composite was larger than either of the component materials or the combination of either two component materials. The authors attributed this behavior to the energy filtering effect due to the barriers at Te-PEDOT:PSS interface and PEDOT:PSS-rGO interface, which were measured to be 0.24 eV and 0.31 eV, respectively. Also, Qiu *et al.* studied the nanocomposite made of poly(3-hexylthiophene) (P3HT) and Bi₂Te₃ nanowires.[74] The authors attribute the high power factor of 13.6 $\mu\text{W}/\text{mK}^2$ to the strongly scattered low energy carriers as potential barrier at the P3HT-Bi₂Te₃ interface was engineered appropriately. However, in spite of the attempts to quantify barrier heights, the relationship between the barrier heights and thermoelectric properties was not discussed in depth. In most cases, only descriptive texts and schematic diagrams illustrating energy filtering were presented instead of measurement results. Direct correlation between barrier heights, energy filtering, and electronic parameters like electrical conductivity and thermopower is still deficient.

CHAPTER III

SOLVENT/ACID TREATED THERMOELECTRIC COMPOSITE MADE OF CARBON NANOTUBES FILLED CONJUGATED POLYMER*

3.1 Introduction

Organic thermoelectric materials such as conductive polymers and small molecules are under intensive research efforts. Aside from their advantages of high flexibility, light weight, and cost-effectiveness, organic thermoelectric materials have highly tunable electrical properties with rationally designed synthetic or fabrication routes, making them promising alternatives to their inorganic counterpart. Among others, poly(3,4-ethylenedioxythiophene): poly(styrenesulfonate) (PEDOT:PSS) is one of the most popular organic thermoelectric materials. It affords widely tunable electrical conductivity and thermopower with adjustable doping level by reducing agents[46, 47, 75] or electrochemical routes,[26] and controllable morphology by organic solvents. The electrical conductivity of treated PEDOT:PSS could be improved by as many as 4 orders of magnitude.[76] Treating PEDOT:PSS with acidic solvents was also reported recently with very high electrical conductivity of 2050 S/cm achieved.[77] In addition, it was also shown that thermoelectric performance of PEDOT:PSS can be tuned by controlling its pH value.[78] Despite these reported TE properties improvement, the underlying

* Reprinted with permission from J.-H. Hsu, W. Choi, G. Yang, C. Yu, Origin of unusual thermoelectric transport behaviors in carbon nanotube filled polymer composites after solvent/acid treatments, *Org. Electron.*, 45, 182-189, Copyright 2017 by Elsevier.

mechanisms for the enhanced performance by polar solvent or acidic solvent treatment have not been fully uncovered. On the other hand, PEDOT:PSS is often hybridized with nano-sized fillers to form nanocomposites. The proposed reasons for enhanced TE properties because of nano-filler incorporation include the improvement of electrical conductivity due to polymer ordering, and the enhanced thermopower due to interface scattering.

In this study, CNT was chosen as a filler for effective charge transport since CNT can strongly interact with conjugated polymers due to the π - π interaction between PEDOT:PSS and CNT.[45] In particular, we studied nontraditional thermoelectric transport behaviors observed from our PEDOT:PSS/CNT composites such as unchanged thermopower despite a large increase of electrical conductivity, an optimum CNT loading to maximize thermopower, and the simultaneous enhancement of electrical conductivity and thermopower, which can remarkably improve thermoelectric performance.

3.2 Experimental

3.2.1 Sample preparation

For the samples with a solvent or acid treatment, 1-g PEDOT:PSS solution (CLEVIOS™ PH 1000, H. C. Starck, solid contents: 1.3%) was mixed with 50-mg dimethyl sulfoxide (DMSO) (99.9%, Mallinckrodt Chemicals) or 55-mg formic acid (FA) (97%, Alfa Aesar) by overnight stirring at room temperature. To synthesize PEDOT:PSS/CNT composites, single-wall CNT (P2 grade, carbonaceous purity >90%,

metal contents of 4–8 wt%, average diameter of ~1.5 nm, Carbon Solutions, Inc.) of 5.9, 12.1, 18.6, 40.0, or 65.0 mg was added to 20-mL PEDOT:PSS solution to vary the CNT wt% in the composites, and then sonicated the mixture with a pen-type sonicator (Misonix Microson XL2000, 10 W) for 2 h and an ultrasonic bath (Branson 1510) for 6 h for dispersion.

Cleaned glass slides (8 mm × 24 mm) were treated with UV-ozone cleaner (Bioforce Nanosciences) for 30 min. Then the PEDOT:PSS or PEDOT:PSS/CNT solution with/without the treatment (0.4 mL) was drop-casted on the glass slides and dried on a hot plate at 90 °C for 1 h. The treated samples were immersed in DMSO or FA for 4 h and then dried at 90 °C on hot plate for 20 min. Typical film thickness was measured to be 4-5 μm using a profilometer (Bruker DektakXT).

3.2.2 Thermopower and electrical conductivity measurements

Samples prepared on glass slides were suspended between two thermoelectric devices (Marlow Industries). One of the thermoelectric devices was cooled while the other was heated to create temperature gradients along the long side of the samples. Temperature differences were measured using two T-type thermocouples (consisting of copper and constantan wires) mounted on both ends of the samples by silver paint. Thermoelectric voltage was measured by the copper wires in the T-type thermocouples. This configuration ensures that temperature and voltage are measured at the same location. The maximum temperature differences were set to 6 K (+3 K ~ -3 K with respect to room temperature), and thermoelectric voltages at 6-8 different temperature

differences were obtained. Then, thermopower values were determined from the slope of the linear relation between thermoelectric voltages and temperature differences. For electrical conductivity measurements, two additional electrical contacts were created at the two ends of the sample to have four-point probe configurations together with the copper wires in the thermocouples. By applying current with the outer two electrical contacts and measuring voltage with the inner two thermocouples, we obtained current-voltage relationships and then their slopes were used to find electrical conductivity.

It should be noted that all of our samples were baked in an oven to avoid a large amount of moisture in the samples. It was found that humidity mainly changes thermopower of PEDOT:PSS but minimally alters its electrical conductivity.

Considering the humidity level is ~50 RH% during our measurements, our measured value (36 $\mu\text{V/K}$) for pristine PEDOT:PSS is close to the literature values. Nevertheless the influence of humidity on the electrical properties of our “composites” is negligible. The electrical conductivity (0.31 S/cm) of pristine PEDOT:PSS is much lower than 4.0 and 16 S/cm respectively for composites containing 6.7-wt% and 20-wt% CNT.

According to the parallel resistor model with PEDOT and CNT,[79] the contribution from PEDOT:PSS on the composite properties is small due to its low electrical conductivity. When the measurements were performed under similar humidity levels, the thermopower of pristine PEDOT:PSS was increased with the addition of CNT, suggesting the change in thermopower is mainly from CNT.

3.2.3 X-ray photoelectron spectroscopy (XPS)

XPS (DAR 400, Omicron) with Mg K_{α} X-ray sources was used to determine the relative amount of PEDOT to PSS. The base pressure and operation pressure are 3×10^{-10} Torr and 1×10^{-9} Torr, respectively. Samples for XPS were prepared by drop-casting the solutions on ITO substrates (Nanocs) with the recipes specified in the sample fabrication section. The survey scans were collected with 1.0 eV resolution followed by high-resolution scans of S 2p with 0.05 eV resolution. Peak fitting was performed by using CasaXPS program with asymmetric Gaussian/ Lorentzian and Shirley background functions.

3.2.4 Tunneling atomic force microscopy

PeakForce tunneling atomic force microscopy (PF-TUNA) (Dimension Icon, Bruker) was used to obtain surface topography as well as current mapping. Images were obtained with a Pt/Ir coated AFM tip (PF-TUNA model, Bruker). The samples were prepared on gold-coated silicon substrates instead of glass substrates using the same materials described in the sample preparation section. Spin-coating was used instead of drop-casting to make thin films for proper measurements. The thickness of gold layer on silicon was 20 nm and titanium was used as an adhesion layer. A voltage bias of 1 V was used to get the TUNA current mapping images.

3.2.5 Hall measurements

Hall measurements were performed following the ASTM F76-08 method at room temperature. A custom-made setup employing the Van der Pauw geometry under 1-T magnetic field was used. Samples were prepared on square (15 mm × 15 mm) glass substrates. After obtaining sheet resistance (R_s) of the samples, Hall mobility (μ) was obtained using the following relation.

$$\mu = |V_H| / (IBR_s)$$

where $|V_H|$, I , and B , are Hall voltage, current, and magnetic field, respectively. The carrier concentration (n) was determined by:

$$n = IB / (q|V_H|d)$$

where q and d are electron charge and sample thickness, respectively.

When composites contain macroscopically inhomogeneous materials, Hall measurement results are unlikely to generate correct values because charge transport occurs through the percolated network of the inclusion upon imposing a magnetic field due to macroscopic inhomogeneity, as shown in the illustration (Figure 5(a)). In our samples, however, the feature sizes of the fillers in our composites are much smaller compared to the size of our composites for the Hall measurements. CNTs are several microns long and on the order of 10 nm (bundles) in diameter. The sample we used for the Hall measurement was 1 cm by 1 cm. Therefore, we believe we can reasonably assume that electrons are deflected under a magnetic field like typical materials used for the Hall measurements, as illustrated in Figure 5(b). Furthermore, our objective of carrying out the Hall measurements is to see the “changes” in carrier concentration and

mobility values with DMSO and FA, rather than reporting the actual values. We believe that the measurement results are meaningful in this sense although we cannot guarantee the accuracy of the actual numbers.

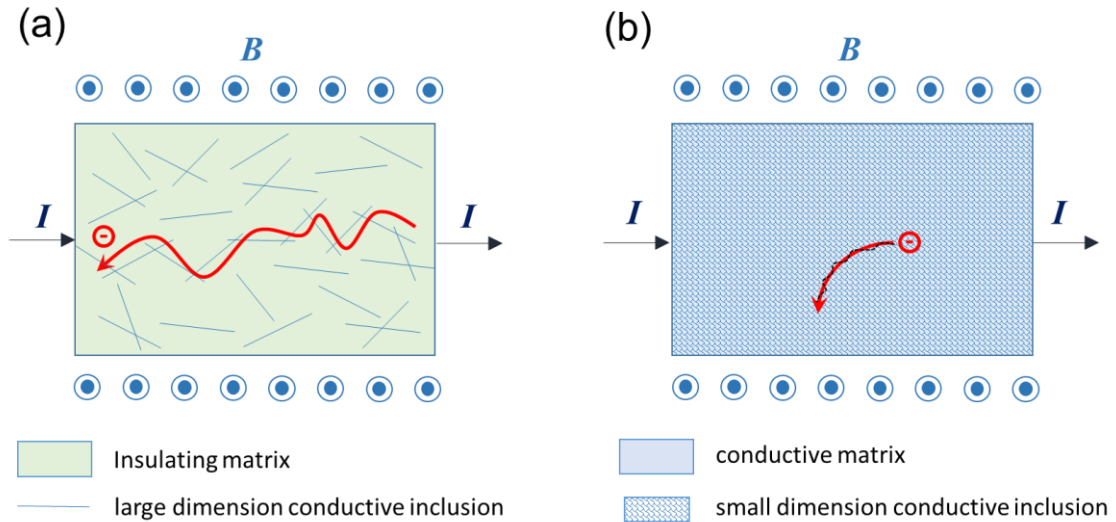


Figure 5. (a) Transport of charge carriers under a magnetic field (B) in a macroscopically “inhomogeneous” composite with an insulating matrix and conducting inclusions. Due to the large dimension of the inclusion and the insulating matrix, the transport path is limited along the percolated networks of the conducting inclusions, showing non-ideal Hall effects. (b) Transport of charge carriers under a magnetic field in a macroscopically “homogeneous” composite with a conductive matrix and conducting inclusions. The small dimension of the inclusion and the conductive matrix minimally influences the transport path of the charge carrier. For instance, the zigzag-shape black line may indicate non-ideal charge transport, but the overall path (red line) is similar to that from typical Hall effects.

3.2.6 Thermopower of composites

The thermopower of composites with the varying volume fraction of conducting particles in an insulating (or significantly less conducting) matrix is unchanged, as shown in the example below. Suppose that gold particles are embedded in an insulating

polymer matrix. The gold particles form one (Figure 6(a)), two (Figure 6(b)), three (Figure 6(c)), or some (Figure 6(d)) percolated chains from the left hand side to the right hand side.

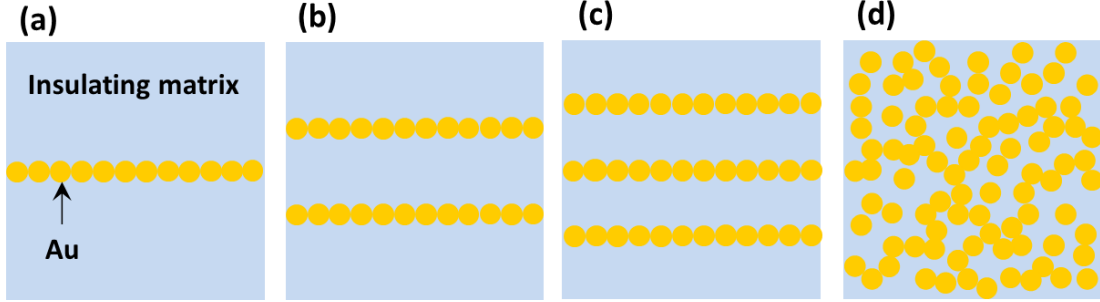


Figure 6. Composites consist of conducting gold particles and an insulating polymer matrix. The gold particles form one (a), two (b), three (c), or some percolated chains (d).

The concentration of the conducting particles in the composites shown in Fig. S2 is different, but the thermopower values of the samples are identical under the assumption of no contact resistance between the gold particles:

$$S_a \approx S_b \approx S_c \approx S_d \approx S_{Au}$$

To calculate the thermopower of the composite, a parallel resistor model[79] can be used:

$$S_{Composite} = \frac{\frac{S_{Au}}{R_{Au}} + \frac{S_{Matrix}}{R_{Matrix}}}{\frac{1}{R_{Au}} + \frac{1}{R_{Matrix}}}.$$

Since $R_{matrix} \gg R_{Au}$, we know that

$$\frac{1}{R_{matrix}} \ll \frac{1}{R_{Au}}.$$

Thus

$$S_{composite} = S_{Au} + S_{matrix} \cdot \left(\frac{R_{Au}}{R_{matrix}} \right).$$

Since

$$\frac{R_{Au}}{R_{matrix}} \ll 1,$$

the thermopower of the composite can be expressed as:

$$S_{Composite} \approx S_{Au}$$

3.2.7 PEDOT:PSS/DWCNT-DMSO composites

Double-wall CNT (carbonaceous purity of 99.9 wt %, Continental Carbon Nanotechnology) was used to synthesize PEDOT:PSS/DWCNT-DMSO composites with various CNT concentrations following the procedures described in the sample preparation section. According to the product sheet, DWCNTs were synthesized by CVD method and contain two concentric tubes with inner-tube diameters of 0.9-2.4 nm and outer-tube diameters of 1.5-3.0 nm with some single- and triple-wall tubes as impurities.

3.2.8 Error analysis for electrical conductivity, thermopower, and the power factor

When an experimental result r is a function of measured variables X_i ,

$$r = r(X_1, X_2, \dots, X_J)$$

The uncertainty can be expressed as:[80]

$$U_r^2 = \left(\frac{\partial r}{\partial X_1} \right)^2 U_{x_1}^2 + \left(\frac{\partial r}{\partial X_2} \right)^2 U_{x_2}^2 + \dots + \left(\frac{\partial r}{\partial X_J} \right)^2 U_{x_J}^2$$

We divide each term in the equation by r^2 ; on the right hand side, we multiply by $(X_i/X_i)^2$ to obtain:

$$\left(\frac{U_r}{r}\right)^2 = \left(\frac{X_1}{r} \frac{\partial r}{\partial X_1}\right)^2 \left(\frac{U_{X_1}}{X_1}\right)^2 + \left(\frac{X_2}{r} \frac{\partial r}{\partial X_2}\right)^2 \left(\frac{U_{X_2}}{X_2}\right)^2 + \dots + \left(\frac{X_J}{r} \frac{\partial r}{\partial X_J}\right)^2 \left(\frac{U_{X_J}}{X_J}\right)^2$$

where U_r/r is the relative uncertainty of the result, and factors U_{X_i}/X_i are the relative uncertainty of each variable. The expression of resistance is:

$$R = \rho \frac{L}{A} = \frac{1}{\sigma} \frac{L}{A}.$$

Thus the electrical conductivity (σ) is:

$$\sigma = \frac{1}{R} \frac{L}{A} = \frac{I}{V} \frac{L}{A} = \frac{I}{V} \frac{L}{Wt}$$

where R, L, A, I, V, W, t are sample resistance, length, cross sectional area, current, voltage, width, and thickness, respectively. The relative uncertainty of electrical conductivity is given by

$$\begin{aligned} \left(\frac{U_\sigma}{\sigma}\right)^2 &= \left(\frac{I}{\sigma} \frac{\partial \sigma}{\partial I}\right)^2 \left(\frac{U_I}{I}\right)^2 + \left(\frac{V}{\sigma} \frac{\partial \sigma}{\partial V}\right)^2 \left(\frac{U_V}{V}\right)^2 + \left(\frac{L}{\sigma} \frac{\partial \sigma}{\partial L}\right)^2 \left(\frac{U_L}{L}\right)^2 + \left(\frac{W}{\sigma} \frac{\partial \sigma}{\partial W}\right)^2 \left(\frac{U_W}{W}\right)^2 \\ &+ \left(\frac{t}{\sigma} \frac{\partial \sigma}{\partial t}\right)^2 \left(\frac{U_t}{t}\right)^2 = \left(\frac{U_I}{I}\right)^2 + \left(\frac{U_V}{V}\right)^2 + \left(\frac{U_L}{L}\right)^2 + \left(\frac{U_W}{W}\right)^2 + \left(\frac{U_t}{t}\right)^2 \end{aligned}$$

From at least 10 measurements, the relative uncertainties of measured parameters were $U_I/I = 0.0013$, $U_V/V = 0.022$, $U_L/L = 0.062$, $U_W/W = 0.072$, and $U_t/t = 0.11$. Then U_σ/σ was calculated to be 0.15. Similarly, thermopower is given by

$$S = \frac{V}{T}$$

where T is temperature difference. The relative uncertainty of thermopower can be obtained by

$$\left(\frac{U_S}{S}\right)^2 = \left(\frac{V}{S} \frac{\partial S}{\partial V}\right)^2 \left(\frac{U_V}{V}\right)^2 + \left(\frac{T}{S} \frac{\partial S}{\partial T}\right)^2 \left(\frac{U_T}{T}\right)^2 = \left(\frac{U_V}{V}\right)^2 + \left(\frac{U_T}{T}\right)^2$$

The relative uncertainty for temperature difference, $U_T/T = 0.073$. U_S/S is calculated to be 0.076.

The power factor (PF) is given by

$$PF = \sigma S^2 = \left(\frac{I}{V} \frac{L}{Wt}\right) \left(\frac{V}{T}\right)^2 = \frac{ILV}{WtT^2}$$

The relative uncertainty of power factor can be obtained by

$$\begin{aligned} \left(\frac{U_{PF}}{PF}\right)^2 &= \left(\frac{I}{PF} \frac{\partial PF}{\partial I}\right)^2 \left(\frac{U_I}{I}\right)^2 + \left(\frac{L}{PF} \frac{\partial PF}{\partial L}\right)^2 \left(\frac{U_L}{L}\right)^2 + \left(\frac{V}{PF} \frac{\partial PF}{\partial V}\right)^2 \left(\frac{U_V}{V}\right)^2 \\ &+ \left(\frac{W}{PF} \frac{\partial PF}{\partial W}\right)^2 \left(\frac{U_W}{W}\right)^2 + \left(\frac{t}{PF} \frac{\partial PF}{\partial t}\right)^2 \left(\frac{U_t}{t}\right)^2 + \left(\frac{T}{PF} \frac{\partial PF}{\partial T}\right)^2 \left(\frac{U_T}{T}\right)^2 \\ &= \left(\frac{U_I}{I}\right)^2 + \left(\frac{U_L}{L}\right)^2 + \left(\frac{U_V}{V}\right)^2 + \left(\frac{U_W}{W}\right)^2 + \left(\frac{U_t}{t}\right)^2 + 4\left(\frac{U_T}{T}\right)^2 \end{aligned}$$

Thus U_{PF}/PF was calculated to be 0.21.

3.3 Results and discussion

3.3.1 Microscopic morphology of PEDOT:PSS/CNT composites

We have synthesized PEDOT:PSS/CNT composites whose CNT wt% is 2.2, 4.4, 6.7, 13.3, or 20 using DMSO (polar solvent) or formic acid (FA) (acid) treated PEDOT:PSS. We also prepared PEDOT:PSS without CNT as well as PEDOT:PSS/CNT composites without DMSO/FA treatment. Figure 7 shows the cold-fractured cross

sections of pristine PEDOT:PSS and PEDOT:PSS/CNT composite films. CNTs were pulled out from the surface during the cold-fracturing process, so more CNTs are shown for the samples with higher CNT concentrations. CNTs are seen more or less uniformly over the surface of the cross section, but it appears that the 20-wt% CNT composite contains aggregated CNTs, as shown in the inset of Figure 7(d).

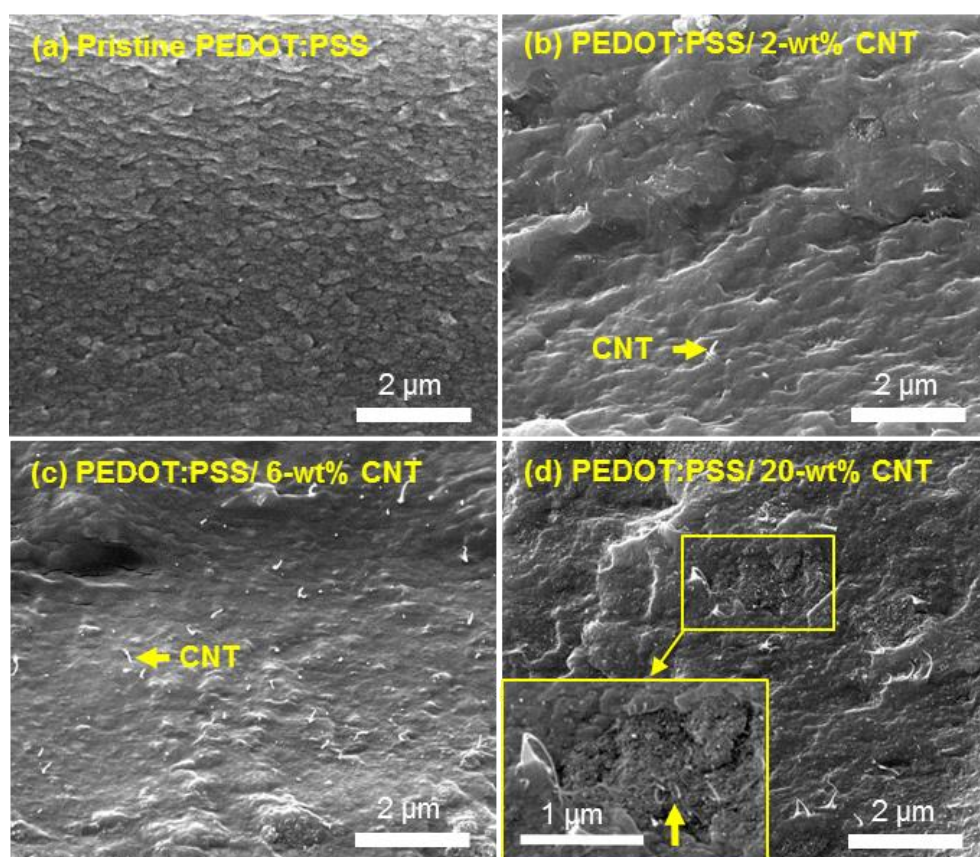


Figure 7. SEM images of cold-fractured cross sections of pristine PEDOT:PSS (a) and PEDOT:PSS/CNT composites containing 2-wt% CNT (b), 6-wt% CNT (c), and 20-wt% CNT (d). The inset shows a portion contains aggregated CNTs.

Figure 8 shows the tunneling atomic force microscope (TUNA) images of PEDOT:PSS/CNT composites without solvent/acid treatment. With higher CNT

concentrations, the number of brighter lines (higher TUNA current) increased, suggesting CNT is better for electron transport compared to PEDOT:PSS. It is also possible that PEDOT:PSS near CNTs become a better electrical conductor because the crystallinity of conducting polymers near CNTs could be improved due to the π - π interaction.[45, 81] When CNT wt% is only 2.2, only small number of bright lines (indicating CNT) were observed (Figure 8(a)), and most of CNTs were disconnected. With 6.7 wt% CNT, thin and long bright lines were clearly seen, and some of them were percolated (Figure 8(b)). When CNT wt% was raised to 20, many of CNTs were connected (Figure 8(c)).

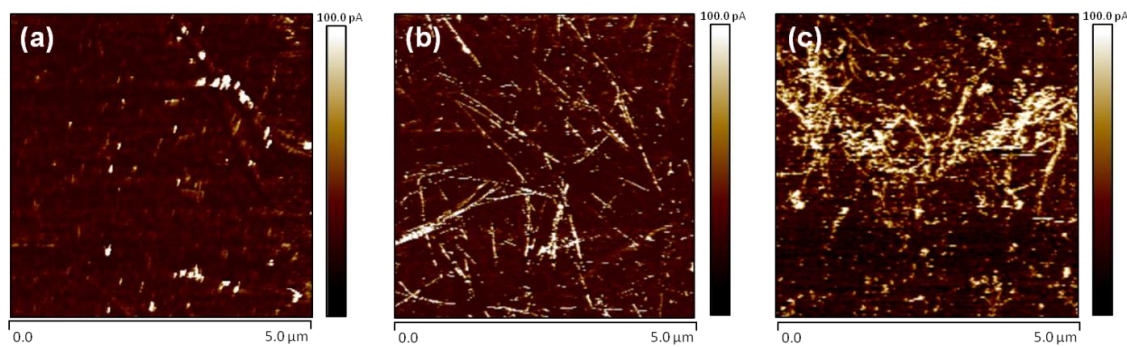


Figure 8. TUNA current mapping of PEDOT:PSS/CNT composites whose CNT concentration is 2.2 wt% (a), 6.7 wt% (b), and 20 wt% (c). Brighter lines indicate more conducting CNTs and the darker background corresponds to PEDOT:PSS whose electrical conductivity is lower than that of CNT.

3.3.2 Thermoelectric properties of PEDOT:PSS/CNT composites

The CNT addition to PEDOT:PSS increased electrical conductivity (Figure 9(a)), and a noticeable increase in electrical conductivity of the composites prior to the treatment was observed from 6.7-wt% CNT loading where percolated CNTs were seen

(green diamond symbol in Figure 9(a)). When DMSO or FA treatment was performed, the electrical conductivity of pristine PEDOT:PSS (0% CNT) was remarkably improved from 0.31 S/cm to 9.9×10^2 S/cm for DMSO-treated sample and 1.1×10^3 S/cm for FA-treated sample (Figure 9(a)). CNT addition further enhanced the electrical conductivity, reaching $\sim 1.8 \times 10^3$ S/cm with 20 wt% CNT. The high electrical conductivity could be ascribed to well percolated and electrically connected CNTs. The more, thicker, and brighter lines in Figure 8(c) from the sample with 20 wt% CNT suggest that carrier transport was greatly facilitated through the CNT network. It should be noted that the electrical properties of our composites is negligibly affected by humidity (see details in section 3.2.2).

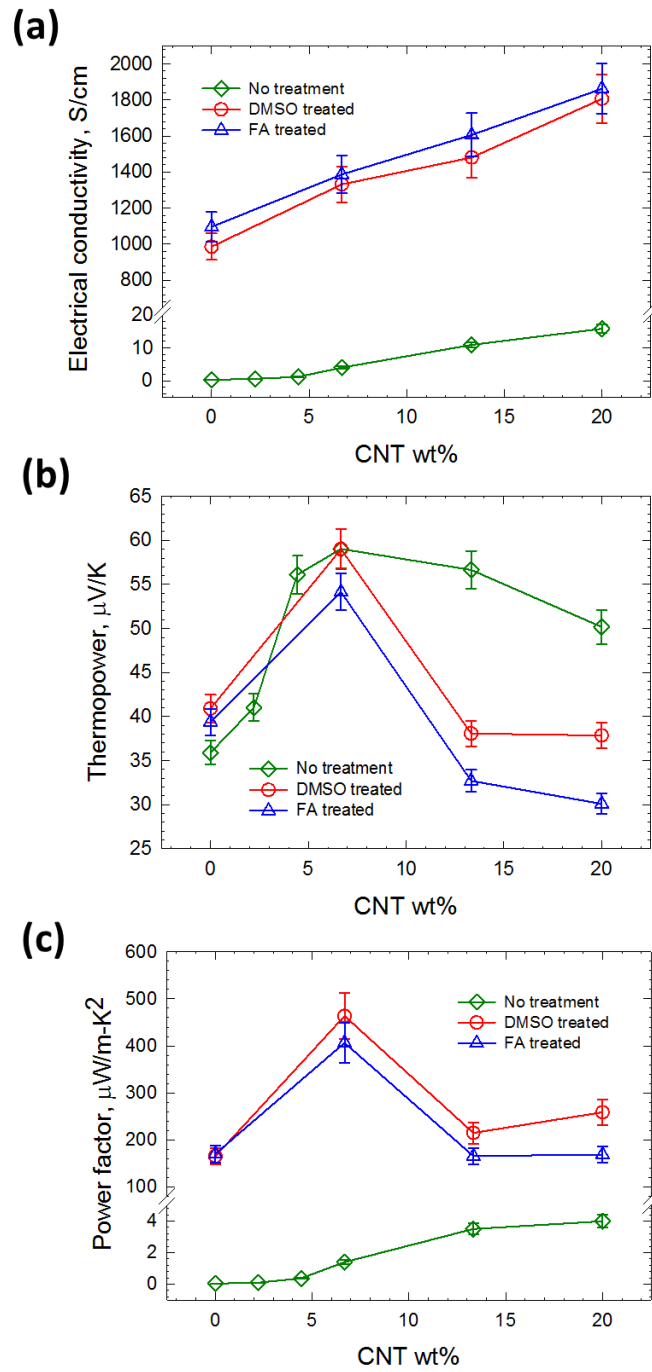


Figure 9. Electrical conductivity (a), thermopower (b), and power factor (c) of PEDOT:PSS/CNT composites when the CNT concentration was varied from 0 to 20 wt% before and after DMSO/FA treatments.

While the electrical conductivity was monotonically increased, the thermopower of the pristine PEDOT:PSS (36 $\mu\text{V/K}$) was raised with the addition of CNT up to 59 $\mu\text{V/K}$ at 6.7 wt% CNT and then decreased with more CNT to 50 $\mu\text{V/K}$ at 20 wt% CNT (Figure 9(b)). The highest thermopower for the samples with DMSO or FA treatment was also observed at 6.7 CNT wt%. Surprisingly, thermopower before and after the DMSO or FA treatment was similar despite large increase (up to a factor of ~ 330) in electrical conductivity after the treatments. It should be noted that traditional inorganic thermoelectric materials show a large reduction in thermopower when electrical conductivity is raised.[82, 83] The power factor (Figure 9(c)) became the highest at this CNT concentration (6.7 wt% CNT), which are larger (464 and 407 $\mu\text{W/m-K}^2$ after DMSO and FA treatment, respectively) than or comparable to those from most of “fully organic” thermoelectric materials.[56, 84-89]

Three intriguing questions arise from the electrical transport behaviors: (1) What is the origin of the large increase in electrical conductivity for the composites treated with DMSO or FA?; (2) Why was the thermopower of DMSO or FA-treated samples unchanged despite the large increase in electrical conductivity?; and (3) Why was the thermopower maximized at a particular CNT loading despite the monotonically increasing electrical conductivity?

3.3.3 Origin of largely increased electrical conductivity after solvent/acid treatment

To answer the first question, we performed x-ray photoelectron spectroscopy (XPS) measurements for pristine PEDOT:PSS, PEDOT:PSS-DMSO, and PEDOT:PSS-

FA (Figure 10). The peaks for the S 2p spectra can be fitted by two component peaks corresponding to the sulfur atom in PEDOT (centered at 165.0 eV and 163.8 eV) and another two component peaks corresponding to the sulfur atom in PSS (centered at 168.9 eV and 167.8 eV), respectively.[90] The peak areas were used to estimate the relative amount of PEDOT and PSS, as summarized in Table 3. It was found that the pristine PEDOT:PSS has a large fraction of PSS (72 %). After the DMSO and FA treatment, PEDOT was increased from 28 % to 45 % (DMSO) and 51 % (FA), indicating that PSS was partially removed after the treatment. Note that the numbers are to compare the change in the relative amount of PEDOT and PSS rather than the accurate quantity of each species. It is worth noting that PEDOT:PSS were treated with DMSO/FA by rigorous overnight stirring prior to the casting process to make the samples, and thus the PSS removal is expected to be uniform throughout the sample (not only the surface).

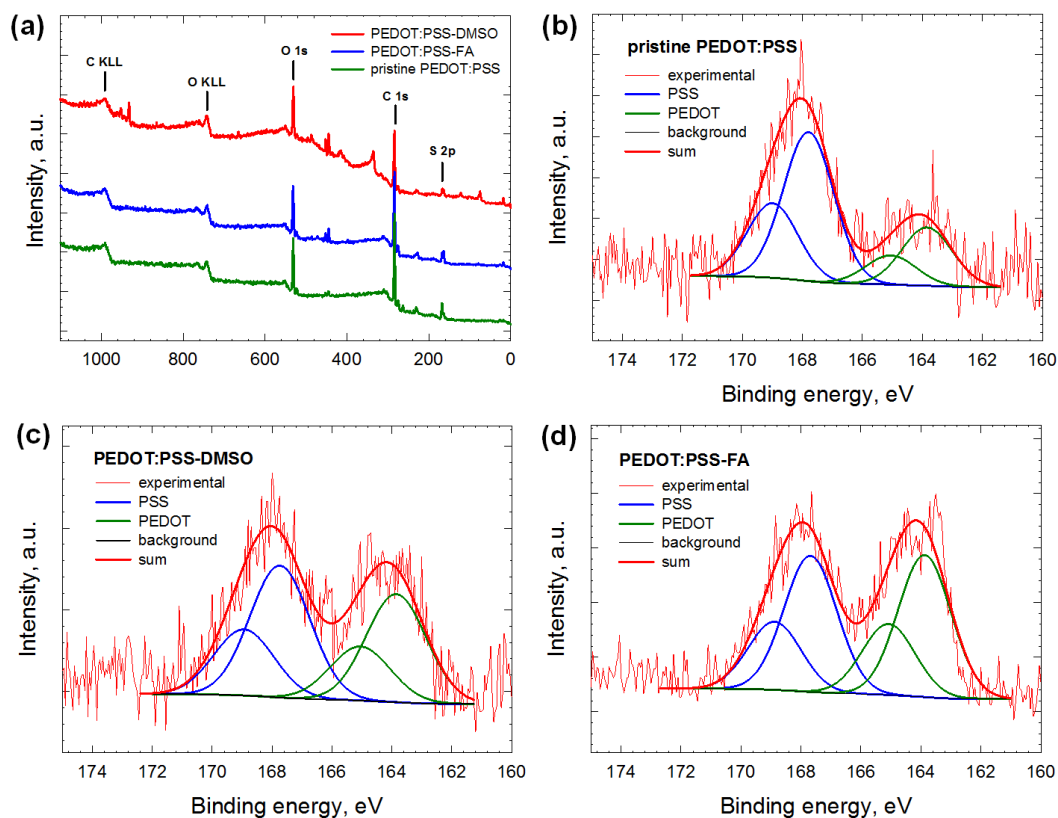


Figure 10. (a) XPS survey scan of PEDOT:PSS before and after the DMSO or FA treatment. S 2p XPS spectra of pristine PEDOT:PSS (b), PEDOT:PSS treated by DMSO (c), and PEDOT:PSS treated by FA (d). The fitted peaks and the component peaks for sulfur in PEDOT (165 eV and 163.8 eV) and PSS (167.8 eV and 168.9 eV) are also shown.

Table 3 Relative amount of PEDOT and PSS estimated by XPS. A_{PEDOT} and A_{PSS} are respectively the sum of the area of component peaks from PEDOT and PSS.

Sample	A_{PEDOT}	A_{PSS}	PEDOT %	PSS %
Pristine PEDOT:PSS	906	2318	28	72
PEDOT:PSS-DMSO	1000	1221	45	55
PEDOT:PSS-FA	1730	1659	51	49

It has been considered that PEDOT:PSS grains are composed of electrically conducting PEDOT rich cores surrounded by insulating PSS rich shells.[91, 92] The electrically resistive shell layers suppress charge transport across the grains. Polymer chains of PEDOT and PSS are bound together by van der Waals force as well as Coulombic attraction due to the positive and negative charges respectively on PEDOT and PSS chains.[93] We infer that treating PEDOT:PSS with polar solvent can screen the van der Waals force and the Coulombic attraction, facilitating the PSS removal. In the case of the acid treatment, protons can couple with the negatively charged PSS, weakening the attraction between PEDOT and PSS. The removal of PSS makes conductive PEDOT cores in contact with each other, forming more connected conducting paths. Thus, the electrical conductivity was boosted up after the treatment. In addition to PSS removal, rearrangement of polymer chain conformation[94] or phase separation of PEDOT and PSS[77] could also be the contributing factors that lead to the conductivity improvement after the treatment.

We further scrutinized the morphologies using AFM, and then found that the root-mean-square roughness changed from 1.5 nm for pristine PEDOT:PSS (Figure 11(a)) to 1.1 and 1.0 nm respectively for DMSO (Figure 11(b)) and FA (Figure 11(c)) treated PEDOT:PSS films. The smoothed surfaces can be attributed to the removal of PSS. This is consistent with the XPS results showing that the ratio of PEDOT to PSS for the FA-treated sample was slightly higher than that for the DMSO-treated sample and much higher than that for the pristine sample.

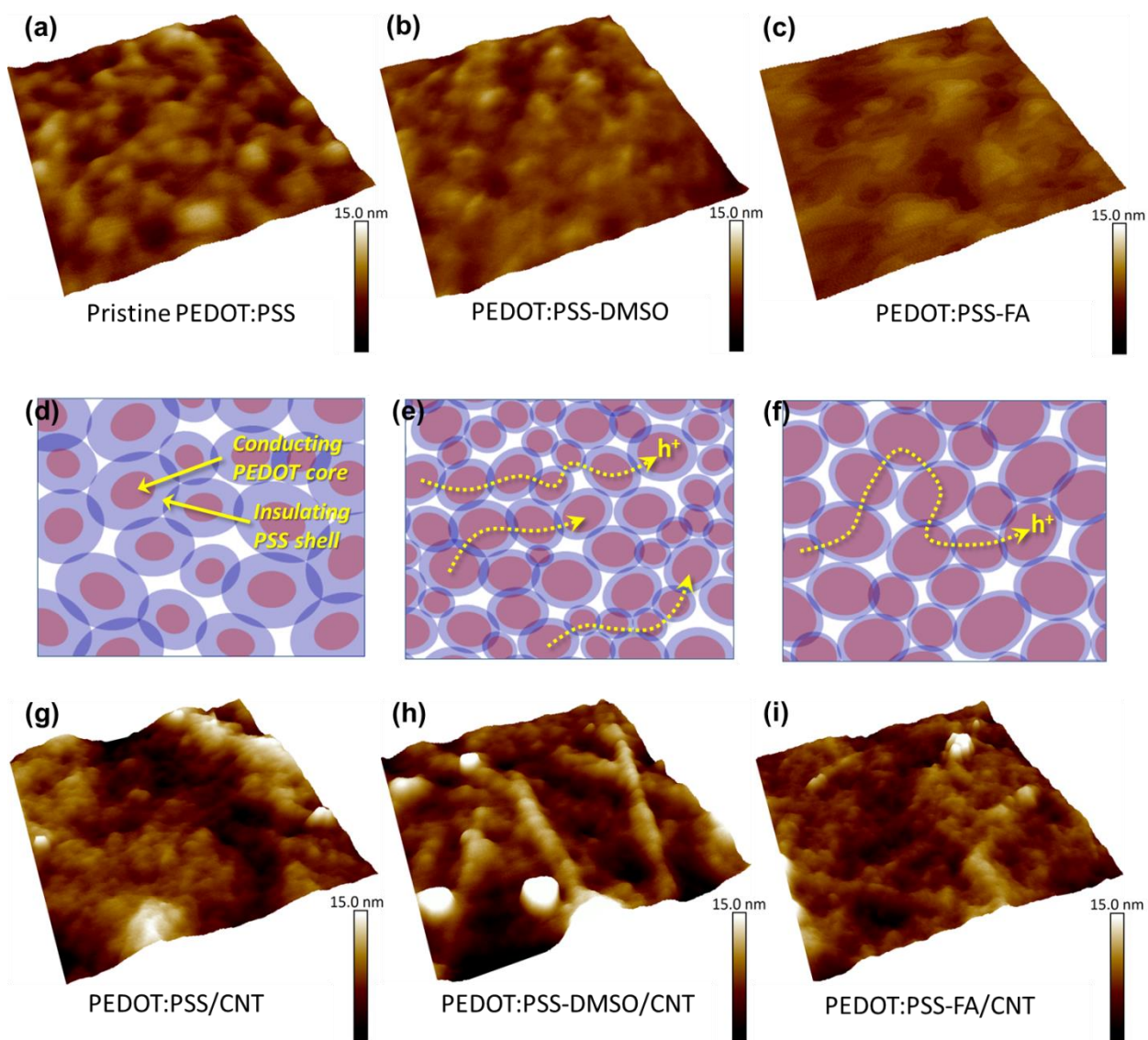


Figure 11. The AFM images of pristine PEDOT:PSS (a) and PEDOT:PSS treated by DMSO (b) and FA (c), and their root-mean-square roughnesses are 1.49, 1.11, and 0.95 nm, respectively. The edge length of the images is 750 nm. The estimated morphology of PEDOT:PSS corresponding to ‘a’, ‘b’, and ‘c’ is illustrated in (d), (e), and (f), respectively. The dashed line indicates hole transport across PEDOT:PSS grains. The smaller grains in ‘e’ have more percolated pathways compared to ‘f’. The AFM images of PEDOT:PSS with 6.67-wt% CNT prior to any treatment (g) and after the DMSO (h) and FA (i) treatment.

3.3.4 Origin of unchanged thermopower after solvent/acid treatment

The large increase in electrical conductivity did not accompany thermopower reduction, which is desirable to improve the thermoelectric power factor. Better understanding of this behavior may lead to even larger improvement in the power factor. To answer the 2nd question, electronic carrier concentration and mobility were determined by the Hall measurement, as shown in Table 4. The DMSO/FA treatment increased both mobility and carrier concentration of pristine PEDOT:PSS. The removal of PSS raises the relative concentration of conducting PEDOT (*i.e.*, increased carrier concentration) as well as results in less interruption by insulating PSS for electronic carrier transport through the conducting PEDOT (*i.e.*, increased mobility).

Table 4 Hall mobility and carrier concentration of the PEDOT:PSS composites with 6.67-wt% CNT and without CNT before and after the DMSO or FA treatment.

Sample	Hall mobility* (cm ² /V-s)	Carrier concentration* (cm ⁻³)
Pristine PEDOT:PSS	0.11	1.3 × 10 ¹⁹
PEDOT:PSS-DMSO	6.5	9.7 × 10 ²⁰
PEDOT:PSS-FA	2.5	2.4 × 10 ²¹
PEDOT:PSS/CNT-DMSO	19	4.0 × 10 ²⁰
PEDOT:PSS/CNT-FA	14	6.0 × 10 ²⁰

* The numbers shown here are for comparison, and may not be very accurate due to the uncertainty of the Hall measurements for composite materials. See section 3.2.5 for more details.

Among the solvent treatments, DMSO-treated PEDOT:PSS showed higher Hall mobility but lower carrier concentration than FA-treated PEDOT:PSS. The higher carrier concentration for FA-treated sample can be ascribed to the more effective removal of PSS (see Table 3). On the other hand, the higher mobility after DMSO treatment could be due to better percolated PEDOT networks caused by smaller granular structure of PEDOT:PSS from the DMSO-treated sample according to Figure 11(b),(c) that qualitatively indicate the grain size from the contrast (height) information. Thus it can be inferred that the smaller grains of DMSO-treated sample have less disconnected PEDOT and a lower chance of having bottleneck-type transport constriction. The morphologies of PEDOT:PSS before and after DMSO and FA treatments are illustrated in Figure 11(d),(e),(f), highlighting thinner PSS after the DMSO/FA treatment, and smaller grain sizes and more percolated PEDOT networks for the DMSO-treated sample compared to the FA-treated sample. There is also a possibility that the higher mobility is originated from extended shape or ordered conformation of PEDOT grains after the solvent (DMSO) treatment,[49, 95, 96] which leads to more percolated networks.

It is worth mentioning our reasoning about relatively unchanged thermopower with the largely increased carrier concentration after DMSO/FA treatments, which is different from the behaviors[82, 83] of typical inorganic thermoelectric materials. When the electrical conduction mainly occurs through PEDOT cores rather than insulating PSS, thermopower is mainly determined by the conducting PEDOT core. Thermopower does not depend on its volume, so a removal of PSS does not affect thermopower. Even for a case that the thermopower of PSS is measured to be high, a high electrical

resistance of PSS makes its contribution to the total thermopower negligible. For PEDOT:PSS, this can be readily understood under an assumption that a parallel resistor model[79, 97] with a conductor and an insulator is valid. More details can be found in section 3.2.6.

When CNT was added to PEDOT, the mobility values of FA (2.5 cm²/V-s) and DMSO (6.5 cm²/V-s) treated PEDOT:PSS were remarkably raised to 14 and 19 cm²/V-s, respectively, resulting in much higher electrical conductivity but negligibly altered thermopower. The large mobility increase can be attributed to the exceptional carrier mobility (up to 10⁵ cm²/V-s) of CNTs.[79, 98] The lower mobility values compared to the intrinsic mobility of CNT may come partly from the intervention of carrier transport by PEDOT:PSS coated on CNTs, as shown in Figure 11(g),(h),(i). It is worth noting that the decreased carrier concentration after the CNT addition comes from the substitution of PEDOT:PSS-DMSO/FA (whose carrier concentration is very high, ~10²¹ cm⁻³) with CNT whose carrier concentration is intrinsically lower (~10¹⁹ cm⁻³).[45, 99]

The increase of mobility rendered thermopower insensitive despite the large increase in electrical conductivity, which can be “qualitatively” understood from the relations between mobility (μ), thermopower (S), and electrical conductivity (σ).[100]

$$\sigma = \mu nq \quad (1)$$

$$S = \frac{1}{qT} \frac{\int \mu(E - E_f) E \frac{\partial f_o}{\partial E} D(E) dE}{\int \mu E \frac{\partial f_o}{\partial E} D(E) dE} \quad (2)$$

where n , q , T , v , E , E_f , f_o , and D are carrier concentration, carrier charge, absolute temperature, carrier velocity, energy, Fermi energy, Fermi-Dirac distribution, and

density of states, respectively. Electrical conductivity is proportional to mobility, as evident from Eq. (1), but the mobility in thermopower (Eq. (2)) appears on both numerator and denominator, minimally affecting thermopower.

3.3.5 Origin of maximized thermopower at intermediate CNT concentration

The last question to answer is why the thermopower was maximized at an intermediate CNT wt% despite monotonically increased electrical conductivity with CNT addition. More CNT addition typically leads to monotonically increased electrical conductivity and monotonically decreased thermopower in a composite.[79, 101, 102] Note that the aggregated CNTs displayed in the composite containing 20 wt% CNT are unlikely to be the origin of the observed behavior since isolated aggregates were sparsely distributed and most of CNTs were more or less uniformly dispersed. Otherwise, electrical conductivity would not continuously increase when more CNTs were added. We suggest a possible scenario, which is an energy filtering effect that could originate from the presence of PEDOT:PSS-CNT junctions in the composite. Energy filtering effect arises when an energy barrier at the interface of two dissimilar materials impedes transport of low energy charge carriers across the interface while allowing high energy carriers to pass.[14, 20, 69-71, 74, 103-106] With proper energy filtering that changes the mean energy of the carriers, it is possible to improve thermopower without significantly sacrificing electrical conductivity.[103]

When CNT was added to PEDOT:PSS, a significant portion of carriers travels through CNTs, as evident from the increased electrical conductivity. Then these carriers

encounter PEDOT:PSS at the junctions between CNTs because PEDOT:PSS are coated on the surface of CNTs, as depicted in Figure 11(g),(h),(i) (the spherical particles are PEDOT:PSS, and brighter lines are CNTs). At low CNT concentrations, most of CNTs are apart, so carrier transport occurs through CNT-PEDOT:PSS-CNT junctions, as illustrated in Figure 12(a). Since the highest occupied molecular orbital (HOMO) of the insulating PSS layer is likely to be located below the Fermi level of CNT, holes (majority carriers) in oxygen-doped p-type CNT (typical CNT stored in air) experience an energy barrier that may impede transport of low energy carriers (Figure 12(c)). As the CNT concentration increases to a level that CNTs are still not in direct contact, more carriers travel through CNTs and thereby this energy filtering effect becomes more pronounced.

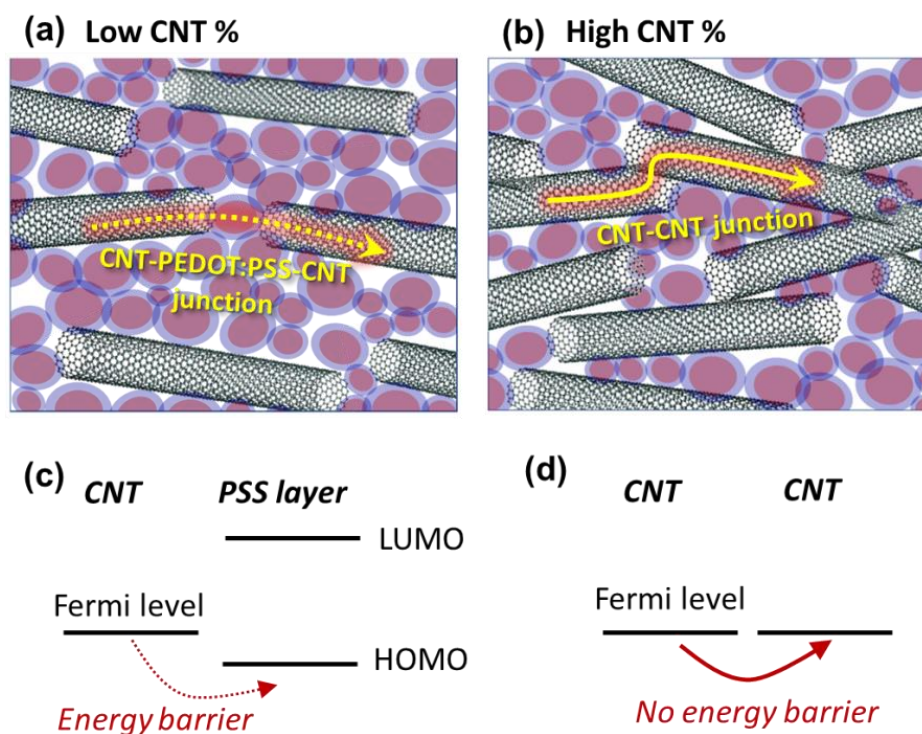


Figure 12. Conceptual illustration of PEDOT:PSS/CNT composites when the CNT concentration is low (a) and high (b). Note that the illustration is not to scale. With a low CNT concentration, carrier transport occurs mainly through CNT-PEDOT:PSS-CNT junctions whereas carriers travel directly through a CNT to another CNT. Energy band diagrams corresponding to ‘a’ and ‘b’ are shown respectively in (c) and (d), suggesting the presence of an energy barrier for the case of ‘a’.

Further increase in the CNT concentration reduces the distance between CNTs as illustrated in Figure 12(b), and thus the effect of PEDOT:PSS-CNT junctions begins to vanish, approaching the intrinsic thermopower of CNT ($\sim 30 \mu\text{V/K}$). [107, 108] When CNTs are in direct contact or bridged by conducting PEDOT core rather than insulating PSS, the energy barrier may become negligible, as illustrated in Figure 12(d). It is worth noting that the thermopower of the FA-treated samples (containing the smallest PSS) at 20 wt% CNT dropped more than those from both samples without the treatment and

with DMSO treatment (Figure 9(b)). The least amount of PSS in the FA-treated sample may have weakened the energy filtering effect. The relatively high thermopower from the composite containing pristine PEDOT:PSS and 15-wt%/20-wt% CNT is another indication that more PSS renders thermopower higher. In AFM images, the CNTs in DMSO/FA-treated samples (Figure 11(h),(i)) are easily seen but the CNTs in the pristine PEDOT:PSS are hardly noticed (Figure 11(g)), suggesting that CNTs in the treated samples are in closer proximity compared to those in the pristine sample.

Therefore, we believe that there is an optimum CNT concentration that makes a significant portion of carriers go through the energy barrier without having CNTs in direct contact or close proximity that vanishes the filtering effects. In our experiments, it appears the optimum CNT concentration is close to 6.7 wt%. This is a case that some CNTs are percolated (see Figure 8(b)), which is between a hardly percolated case (see Figure 8(a)) and a largely percolated case (see Figure 8(c)). Additionally, we synthesized DMSO-treated composites with double-wall CNT containing more metallic tubes. The measured electrical conductivity and thermopower of PEDOT:PSS/DWCNT-DMSO composites (Figure 13) as a function of CNT wt% are similar to those of PEDOT:PSS/CNT-DMSO composites containing single-wall CNTs. This suggests carrier transport is governed by metallic tubes or the CNT used in our experiments was doped to have the Fermi level close to its HOMO like a degenerate or highly-doped semiconductor, which supports our qualitative band diagrams in Figure 12(b),(d).

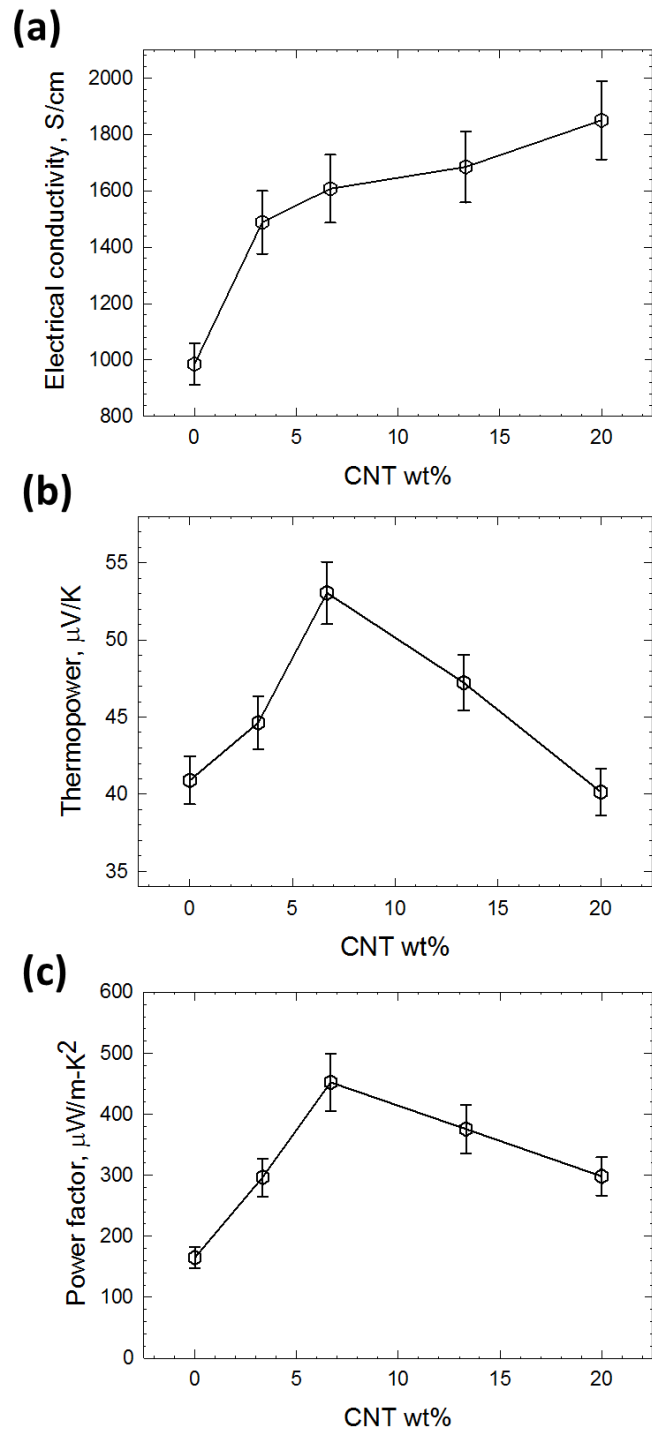


Figure 13. Electrical conductivity (a), thermopower (b), and power factor (c) of DMSO-treated PEDOT:PSS/DWCNT composites with DWCNT concentrations from 0 to 20 wt%.

3.4 Conclusions

In summary, this work investigates the thermoelectric properties of CNT-filled PEDOT:PSS composites with solvent and acid treatments and suggests the origin of unusual electrical transport behaviors – large increase in electrical conductivity for DMSO/FA treated composites; simultaneous increase of thermopower and electrical conductivity; and maximized thermopower at a particular CNT concentration. From XPS, AFM, Hall measurement, and TUNA results, the PSS removal and morphology change for the composites treated with DMSO and FA were suggested as important contributing factors for the unusual electrical transport. Our results indicate that the DMSO/FA treatment mainly removes insulating PSS, improving the carrier mobility and thereby electrical conductivity. However, this PSS removal did not noticeably change thermopower because thermopower is an intrinsic property that does not depend on volume. The energy filtering effect may play a role in maximizing thermopower at an intermediate level of CNT concentration because a moderate level of CNT percolation makes the PEDOT:PSS-CNT junction effect prominent. The highest power factor was observed at an intermediate CNT concentration, which can be mainly attributed to the unchanged thermopower despite large increase in electrical conductivity. We believe this study provides better understanding of polymer/CNT composites and offers possibility for further improvements for TE applications and beyond.

CHAPTER IV
ENERGY BARRIER TUNING AT THE INTERFACE OF ORGANIC
THERMOELECTRIC MATERIALS FOR THERMOELECTRIC PROPERTIES
IMPROVEMENT

4.1 Introduction

From the previous study, it had been revealed that the CNT-PEDOT junctions play an important role in the performance of organic composite thermoelectric materials. With proper number of junctions that form energy barriers in the conductive path of charge carriers, evident thermoelectric properties improvement could be realized presumably due to energy filtering effect. It has been shown theoretically that low energy charge carriers reduce thermopower because the partial contribution of low energy carriers to thermopower is negative.[109] Thus, by introducing energy barriers in material that selectively filter out low energy carrier, thermopower and overall thermoelectric properties could potentially be improved.

Studies about energy filtering have been mainly focus on inorganic materials. Having shown that energy filtering could also play a role in thermopower improvement in organic thermoelectric materials in our previous study, some questions could arise here: what is the correlation between electrical and thermoelectric properties of the materials and the energy barrier height existing at material interface? Is there a proper barrier height that leads to maximized thermoelectric properties? By further delving into these questions, we aim to have a better understanding of energy filtering effect in

organic materials, and to exploit the benefits of energy level engineering to the largest extent. Knowing that barrier height can be controlled by adjusting the relative energy levels (in particular Fermi levels) between materials, and motivated by the literature demonstrating thermoelectric property tuning using organic electrochemical transistor (OECT),[48] in this study, we employed OECT as a vehicle for studying the effect of energy level (or barrier height) modulation on the thermoelectric properties of CNT-PEDOT-CNT junction.

4.2 Experimental

4.2.1 Organic electrochemical transistor (OECT) device fabrication

For fabricating organic electrochemical transistor devices, SWCNT (P2 grade, carbonaceous purity >90%, metal contents of 4–8 wt%, average diameter of ~1.5 nm, Carbon Solutions, Inc.), DWCNT (a purified grade called XBC grade, contains two concentric tubes with inner-tube diameters of 0.9–2.4 nm and outer-tube diameters of 1.5–3.0 nm with some single- and triple-wall tubes as impurities) and MWCNT (8–16 nm) solution were prepared by mixing 10-mg of CNT with 30-mg sodium dodecylbenzenesulfonate (SDBS)(88 %, Acros Organics) and 20-g DI water and then sonicated the mixture with a pen-type sonicator (Misonix Microson XL2000, 10 W) for 2 h and an ultrasonic bath (Branson 1510) for 6 h for dispersion. Then the source, drain, and gate electrodes formed by CNT films were prepared by spraying CNT solution onto pre-cleaned glass substrates (3 inch × 1 inch) masked with Kapton tape at ~80 °C with a spray gun (0.2 mm nozzle diameter, GP-S1, Fuso Seiki Co.), leaving a gap of 3 mm

between source and drain electrodes. The CNT film thickness was measured to be 158 nm. The samples were immersed into DI water overnight for washing our excess SDBS and dried on a hotplate. After removing the mask, the gap between source and drain was then bridged with poly(3,4-ethylenedioxythiophene) : polystyrene sulfonate (PEDOT:PSS) (CLEVIOS™ PH 1000, H. C. Starck, solid contents: 1.3%) by spraying PEDOT:PSS solution pre-doped with 5 wt% dimethyl sulfoxide (DMSO) (99.9%, Mallinckrodt Chemicals) at ~80 °C. Finally, poly(4-styrenesulfonic acid) film (PSSH) (18 wt%, Sigma-Aldrich) film was sprayed on top of the PEDOT region and bridged the PEDOT region and the gate area at room temperature.

4.2.2 Thermopower and electrical conductivity measurements

Thermopower and electrical conductivity were measured in a same way as described in section 3.2.2.

4.2.3 Cyclic voltammetry (CV)

CHI 600 electrochemical workstation was used to carry out the CV experiments. A standard one-compartment and three-electrode cell was used with PEDOT and CNT coated Au films as the working electrode, Ag/AgCl as the reference electrode, and Pt wire as the counter electrode. The electrolyte solution was made of an anhydrous acetonitrile solution (99.8%, Sigma-Aldrich) containing 0.1 M tetraethylammonium perchlorate (TEAP)(98%, Acros Organics). Before testing, the solution was bubbled with 50-sccm N₂ for 20 min to remove oxygen. Ferrocene/ferrocenium (Fc/Fc⁺) redox

couple was used as an external standards for calibrating cyclic voltammetry (CV) curve. The half-wave potential of Fc/Fc⁺ redox couple ($E_{1/2}(\text{Fc}/\text{Fc}^+)$) was obtained from $(E_{ox} + E_{red})/2$, where E_{ox} and E_{red} are the oxidation and reduction peak potentials, respectively. $E_{1/2}(\text{Fc}/\text{Fc}^+)$ was estimated to be -0.04 V.

The HOMO and LUMO levels were determined by the following equations:

$$E_{HOMO} = -(4.8 - E_{1/2, \text{Fc}, \text{Fc}^+} + E_{ox, onset})$$

$$E_{LUMO} = -(4.8 - E_{1/2, \text{Fc}, \text{Fc}^+} + E_{red, onset})$$

where $E_{ox, onset}$ and $E_{red, onset}$ are the onset potential of oxidation and reduction peaks of SWCNT, respectively.

4.2.4 Ultraviolet visible near infrared (UV-vis-NIR) spectroscopy and Tauc plot

CNT films were prepared by spraying SWCNT, DWCNT, and MWCNT solution onto glass substrates, as described in section 4.2.1. UV-vis-NIR spectra of SWCNT, DWCNT, and MWCNT films were obtained using a UV-vis-IR spectrophotometer (Hitachi U-4100). For optical bandgap determination by Tauc plot, with the equation:[110]

$$(\alpha E_{ph})^n = B(E_{ph} - E_g)$$

where E_{ph} is the photon energy, E_g is the optical bandgap, α is the absorption coefficient, which is equal to absorbance divided by film thickness, B is a constant, and $n = 2$ for direct allowed transition, the $(\alpha E_{ph})^2 - E_{ph}$ plot can be made. By finding the crossover

point of the extrapolation line of Tauc plot and the x-axis, the optical bandgap of CNTs can be determined.

4.2.5 Ultraviolet photoelectron spectroscopy (UPS)

UPS results were obtained using Omicron XPS/UPS system. HIS 13 emitting at 21.2 eV (He I radiation) was used as the UV source. Electron analysis was done with Omicron's 124 mm mean radius electrostatic hemispherical dispersive energy analyzer with the 128-channel micro-channelplate Argus detector with 0.8 eV resolution. A gold foil (99.95 %, 0.05 mm thickness, Alfar Aesar) was used as a reference.

4.2.6 Kelvin probe force microscopy (KPFM) measurement

Bruker Dimension Icon atomic force microscope (AFM) was used with a Pt/Ir-coated AFM tip (SCM-PIT model, Bruker). The location of the Fermi energy level was determined by measuring the contact potential difference (CPD), which is the work function (WF) difference between a probe and a sample, in ambient conditions. Since the WF of a probe tip may be affected by humidity and other contaminants in air, the WF of the Pt-coated tip was calibrated by a gold foil (99.95 %, 0.05 mm thickness, Alfar Aesar). The CPD of the gold foil was measured to be -0.37 V. The work function (WF) of the gold foil was estimated to be 5.43 eV with respect to vacuum according to UPS results. Then, the WF of the tip was calculated to be 5.06 eV using the following relation:

$$WF_{tip} = WF_{Au} + CPD_{Au}$$

Note that WF in this relation is a positive number. With WF_{tip} information, WF values of PEDOT and CNTs were estimated using the following relation.

$$WF_{sample} = WF_{tip} - CPD_{sample}$$

4.2.7 Fabricating PEDOT-CNT multi-junction samples by lift-off processes

For fabricating PEDOT/CNT multi-junction samples by lift-off processes, CNT films were prepared by spraying SWCNT solution onto glass substrates, as described in section 4.2.1. The CNT film thickness was measured to be 158 nm. Photoresist (Shipley 1818) was spun coated onto the CNT-sprayed substrates at 1600 rpm for 1 min, and the samples were dried on hotplate at 120 °C for 5 min. Subsequently, 1 to 5 narrow gaps were created in parallel on photoresist/CNT films by scratching the films with razor blade. The gap width was measured to be 70 μ m. Then the samples were treated with UV-ozone cleaner (Bioforce Nanosciences) for 30 min for improving film adhesion deposited in the following step. PEDOT:PSS films doped with 5 wt% DMSO was spun coated onto the samples at 2400 rpm for 1 min and the samples were dried at 120 °C for 20 min. Part of the PEDOT film was lifted-off by immersing the samples into acetone for dissolving the photoresist film for 4 hours. The PEDOT was reduced by treating it with hydrazine (99+%, Alfa Aesar) vapor in a sealed box for 2.5 min. After drying 120 °C for 20 min, the samples of CNT films with 1 - 5 gaps filled with PEDOT:PSS were completed. The schematic fabrication steps for a sample with one junction, as an example, is shown in Figure 14.

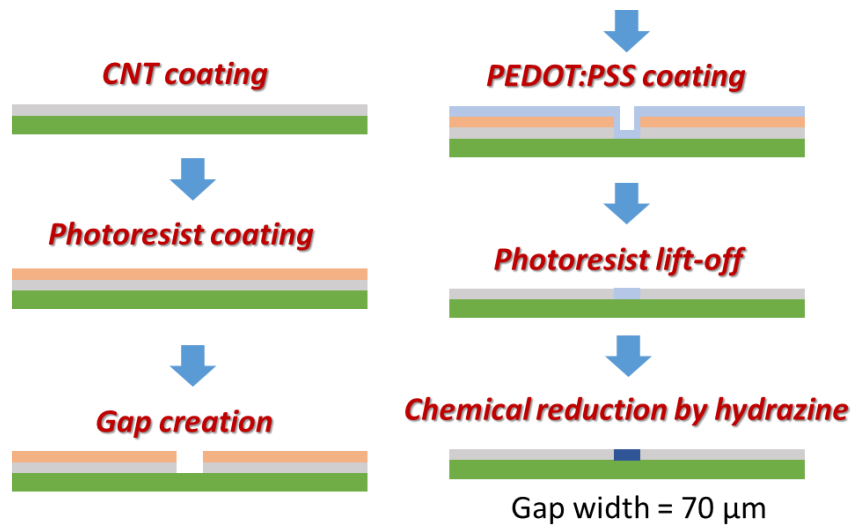


Figure 14. Fabrication steps of PEDOT-CNT multi-junction samples by lift-off processes. One junction sample is shown as an example.

4.2.8 Fabricating PEDOT-CNT multi-junction samples by layered processes

For fabricating PEDOT/CNT multi-junction samples by layered processes, CNT films were prepared by spraying SWCNT solution onto glass substrates masked with tape. The CNT film thickness was measured to be 158 nm. PEDOT:PSS films doped with 5 wt% DMSO was sprayed onto the sample through a shadow mask to overlap the as-deposited CNT film. The PEDOT film thickness was measured to be 55 nm. The PEDOT film was then reduced by treating it with hydrazine vapor in a sealed box for 2.5 min. Then again a CNT film was sprayed on top of the as-deposited PEDOT film to overlap it, and then PEDOT film was sprayed and reduced. The steps were repeated until desired number (1-8) of PEDOT-CNT junctions were reached. The schematic fabrication steps is shown in Figure 15.

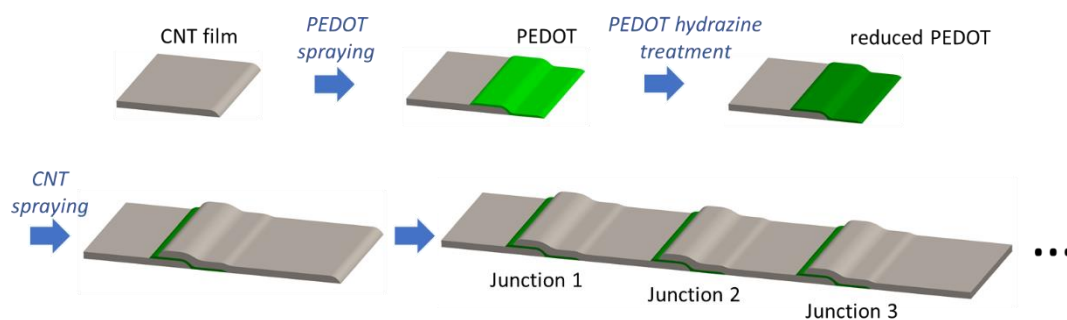


Figure 15. Fabrication steps of PEDOT-CNT multi-junction samples by layered processes.

4.3 Organic electrochemical transistor (OECT) – design, operation, and analysis

Figure 16 shows the design of the OECT device. The source, drain, and gate electrodes were formed by sprayed conductive CNT films, with the gap between source and drain bridged by PEDOT:PSS. The overlap between CNT and PEDOT films was narrow (300 μm). Poly(4-styrenesulfonic acid) (PSSH), as a solid electrolyte, formed on top of the PEDOT region and bridged the gate area. Three kinds of CNTs (single-wall CNT, double-wall CNT, and multi-wall CNT) with different bandgaps and electrical properties were used in this study. In the device, it was designed such that there was a much longer CNT region (60 mm) compared to PEDOT region (3 mm) along the direction of CNT-PEDOT-CNT junction. In this way, when energy levels of PEDOT are modulated by gate voltage, the junction serves as a “switch” of charge carrier flow, controlling thermoelectric properties of the system, and the overall conductivity is not going to be much affected because the PEDOT region is narrow.

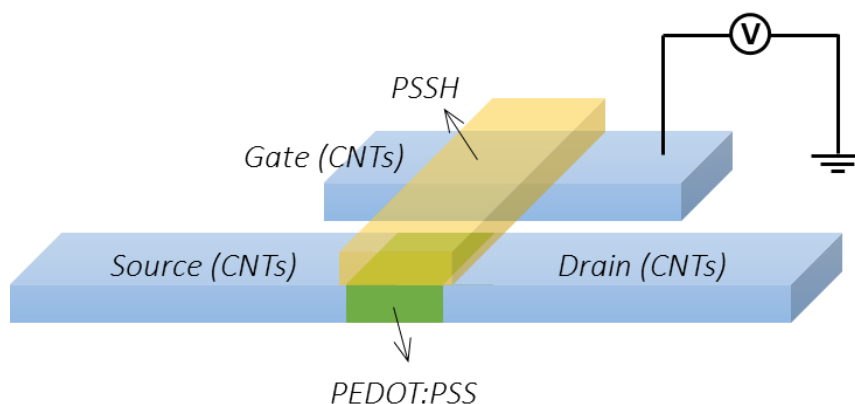
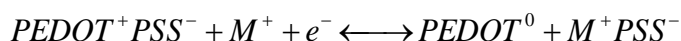


Figure 16. The design of organic electrochemical transistor (OECT) device in this study.

The working principle of the OECT can be described as follows: when operated, the carrier concentration of PEDOT is controlled by the voltage applied to the gate area.[111] As a positive voltage is applied to the gate, positive ion in the polyelectrolyte (H^+ in PSSH) is repulsed by the voltage and can enter the PEDOT film, coupling with the negatively charged PSS^- . The originally positively charged PEDOT is thus reduced and carrier concentration on the PEDOT backbone diminished. In this way, carrier concentration, and thus energy levels of PEDOT can be modulated by the applied gate voltage. The reaction can be expressed by the following equation:[112]



where $PEDOT^+ PSS^-$ is the intrinsically doped conductive PEDOT:PSS with high carrier concentration, M^+ is the counter ion (H^+ in PSSH) from the electrolyte, $PEDOT^0$ is the de-doped PEDOT:PSS with low carrier concentration, and $M^+ PSS^-$ is the PSS molecule coupled with the counter ion.

The OECT containing CNT-PEDOT-CNT junction has several advantages over the PEDOT/CNT composites we previously studied as we investigate the effect of energy level modulation. Firstly, the application of gate voltage with a transistor configuration offers a highly controllable and reversible way for energy level modulation as compared to alternative routes such as chemical doping/de-doping. As compared to traditional transistors, OECT device can be fabricated by much easier solution processes. Gate, source, and drain electrodes can be patterned from a single film.[111] More importantly, as the gate voltage of traditional transistor affects only the material that is in close proximity to the dielectric layer, the gate voltage of the OECT affects bulk material in the channel, ensuring the modulation of energy level to be uniform across the entire PEDOT film.[111] Secondly, the CNT-PEDOT-CNT structure in our OECT device is well defined in terms of dimension and geometry as compared to the randomly oriented CNTs in the CNT/PEDOT composite. Moreover, in the OECT device, the properties of CNT and PEDOT are easy to be fine-tuned and analyzed individually and independently. These advantages render the OECT containing CNT-PEDOT-CNT junction a simple and viable way for studying the effect of energy level modulation in our system.

When positive gate voltage is applied to the OECT, two major factors that lead to thermoelectric properties change should be taken into consideration: change of PEDOT doping level, and change of barrier height between CNT and PEDOT. Considering the first factor, the positive gate voltage will make PEDOT n-doped. Thus, a reduced carrier concentration (and electrical conductivity) and increased thermopower can be expected as long as the material is still p-type (polarity not inverted).[109] For the second factor,

the positive gate voltage alters Fermi level of PEDOT and changes the energy barrier height between CNT and PEDOT, leading to thermoelectric properties change. Barrier height between CNT and PEDOT can be estimated by the geometry of the band diagram, as shown in Figure 17. To transport across the junction, charge carrier (holes) needs to transport from Fermi level (for metallic CNT) or highest occupied molecular orbital (HOMO) (for semiconducting CNT) of CNTs to HOMO level of polymer. If a junction between metallic CNT and PEDOT is considered (Figure 17(a)), given that work function of CNT is larger than the work function of PEDOT (which is mostly the case according to literature, and this will be experimentally verified later), the barrier height between CNT and PEDOT can be expressed as:

$$B = E_{gp} - \varphi_p + \chi_p$$

where B is the barrier height, E_{gp} is polymer bandgap, φ_p is the work function of polymer, and χ_p is the electron affinity of polymer. On the other hand, if a junction between semiconducting CNT and PEDOT is considered (Figure 17(b)), and, again, work function of CNT is larger than the work function of PEDOT, the barrier height can be expressed as

$$B = E_{gp} - E_{gCNT} + \varphi_{CNT} - \varphi_p + \chi_p - \chi_{CNT}$$

where E_{gCNT} is CNT bandgap, φ_{CNT} is the work function of CNT, and χ_{CNT} is the electron affinity of CNT. When a positive gate voltage is applied, Fermi level of PEDOT shifts upward, and φ_p is reduced. As other factors in the barrier height expression remain relatively unchanged (this will be experimentally verified), the barrier height will

increase, leading to reduced electrical conductivity and increased thermopower. Since both factors (change of PEDOT doping level, and change of barrier height) lead to reduced electrical conductivity and increased thermopower as positive gate voltage is applied, relative contribution of the two factors to thermoelectric property change will need to be analyzed to see how energy filtering contributes to thermoelectric properties improvement.

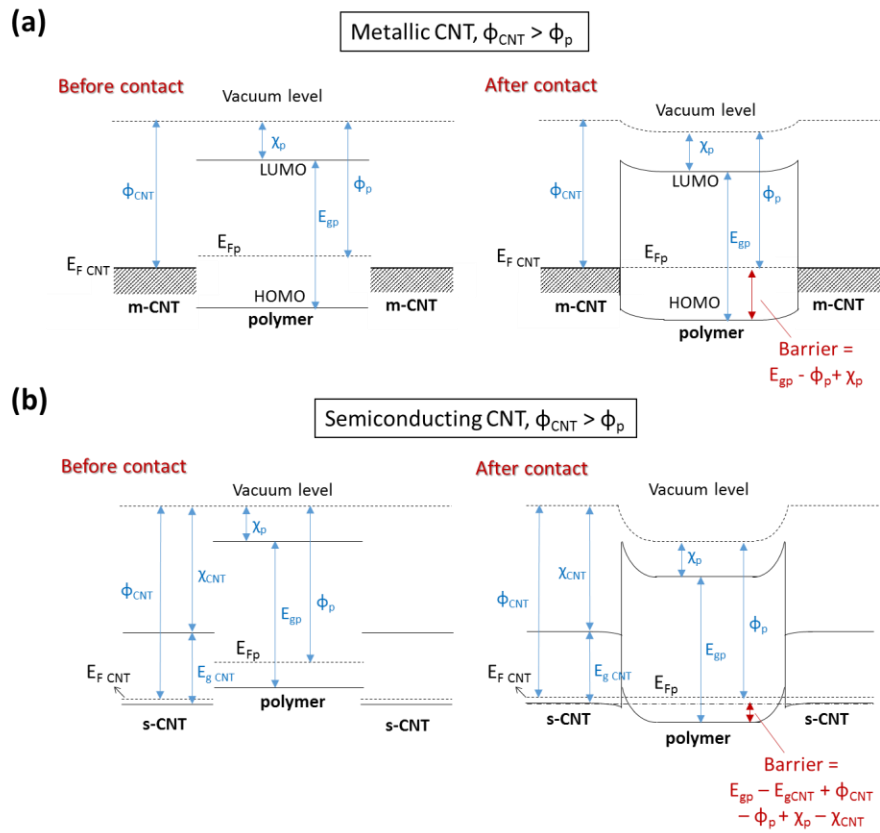


Figure 17. Energy band diagrams showing the barrier height between CNT and PEDOT at different scenarios. For a contact between metallic CNT and PEDOT, given that work function of CNT is larger than that of PEDOT, the barrier height can be expressed as $E_{gp} - \phi_p + \chi_p$. For a contact between metallic CNT and PEDOT, given that work function of CNT is larger than that of PEDOT, the barrier height can be expressed as $E_{gp} - E_{g,CNT} + \phi_{CNT} - \phi_p + \chi_p - \chi_{CNT}$.

In this study, the Fermi level and carrier concentration of PEDOT in the PEDOT-CNT junction was controlled by applying gate voltage. The energy levels of highest occupied molecular orbital (HOMO), lowest unoccupied molecular orbital (LUMO), and the Fermi levels of CNTs and PEDOT with different gate voltage were determined by Kelvin probe force microscopy (KPFM), UV-vis spectroscopy, cyclic voltammetry (CV), and ultraviolet photoelectron spectroscopy (UPS). The band diagrams of the PEDOT-CNT were constructed accordingly and the energy barrier between CNT and PEDOT as a function of applied gate voltage can be estimated. The correlation between energy barrier height and thermoelectric properties was established, and finally, the improvement of thermoelectric properties due to energy filtering was analyzed.

4.4 Results and discussion

4.4.1 Thermoelectric properties of PEDOT-CNT junction in OECT

Figure 18(a) shows the electrical conductivity and thermopower of single wall CNT-PEDOT-CNT device as the function of gate voltage. Power factor as the function of gate voltage is also shown in Figure 18(b). When no gate voltage was applied, the device shows electrical conductivity of 760 S/cm, thermopower of 77.9 $\mu\text{V/K}$, and power factor of 461 $\mu\text{W/m-K}^2$. The thermoelectric performance of the CNT-PEDOT-CNT junction is superior to either of the two components (for SWCNT, the electrical conductivity is 952 S/cm, the thermopower is 63.7 $\mu\text{V/K}$, and the power factor is 386 $\mu\text{W/m-K}^2$; for PEDOT, the electrical conductivity is 655 S/cm, the thermopower is 29.9 $\mu\text{V/K}$, and the power factor is 58.6 $\mu\text{W/m-K}^2$). This is an indication that energy barrier

plays a role in thermoelectric properties improvement. When positive gate voltage was applied, because of the PEDOT was n-doped (decreased carrier concentration), same as our expectation, the electrical conductivity dropped monotonically from 760 S/cm as $V_g = 0$ V to 579 S/cm as $V_g = 20$ V. This accompanied monotonic thermopower increase from 77.9 $\mu\text{V/K}$ as $V_g = 0$ V to 128.2 $\mu\text{V/K}$ as $V_g = 20$ V. The power factor, benefited by the enhanced thermopower with not-so-much decreased conductivity, peaked at 1047 $\mu\text{W/m-K}^2$ as $V_g = 15$ V. This is one of the most decent values achieved by organic thermoelectric materials. For OECTs made of DWCNT and MWCNT, a similar trend of electrical conductivity and thermopower with gate voltage was observed (Figure 18(c),(d),(e),(f)). The notable difference in electrical conductivity of devices made of different kinds of CNTs was due to the largely distinct electrical conductivity of CNT films: the electrical conductivity of SWCNT, DWCNT, and MWCNT films were measured to be 952 S/cm, 2730 S/cm, and 17.3 S/cm, respectively. The huge difference in electrical conductivity of CNT films could originate from different extent of de-bundling when solution processed as well as varied packing density.[108]

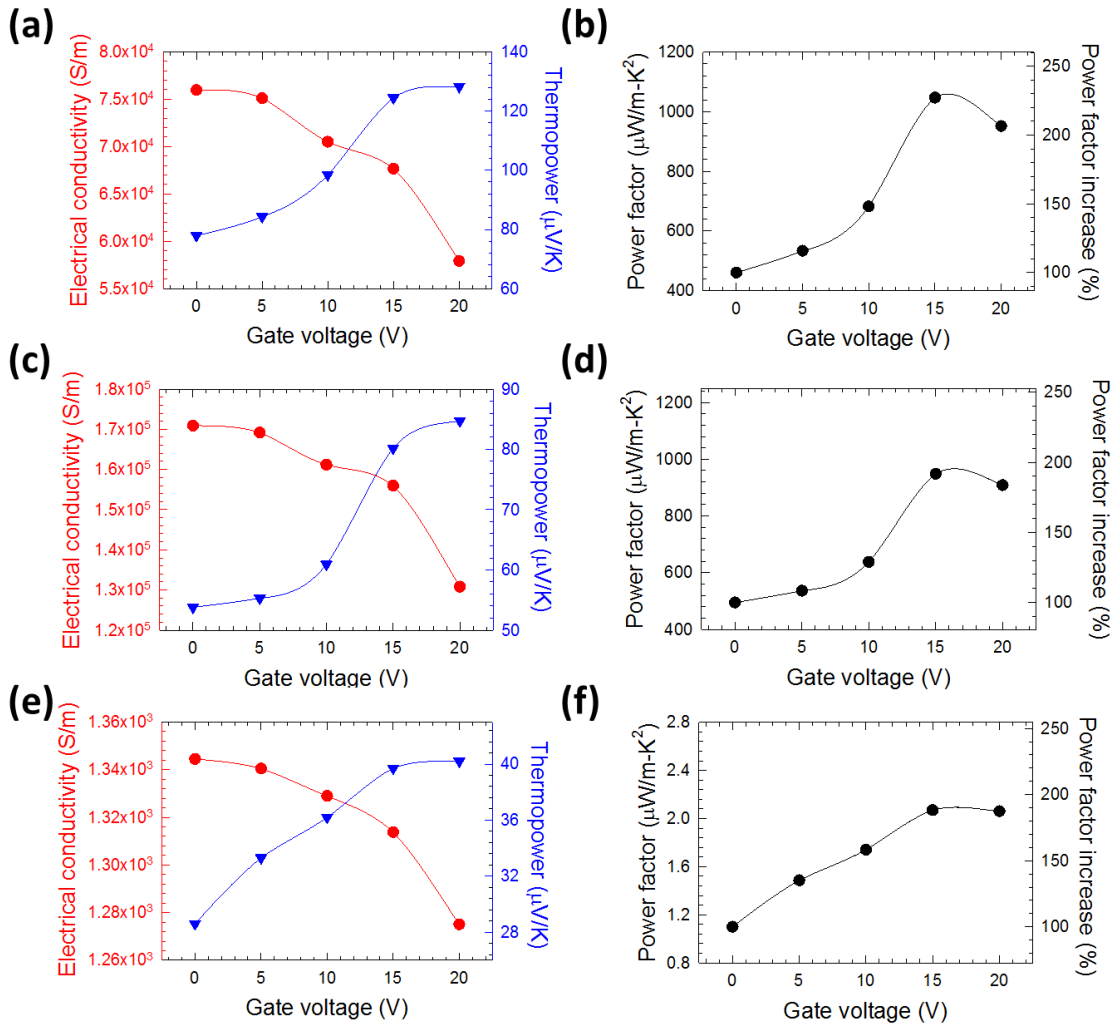


Figure 18. Electrical conductivity, thermopower, and power factor of CNT-PEDOT-CNT junction when SWCNT ((a), (b)), DWCNT ((c), (d)), and MWCNT ((e), (f)) was used for the CNT region.

4.4.2 Band diagram construction

In order to identify the major contributing factor of thermoelectric performance improvement, band diagrams of the PEDOT-CNT junctions were constructed by measuring all the energy levels of respective materials. Taking SWCNT as an example, Figure 19(a) shows the CV curve for HOMO/LUMO determination. HOMO and LUMO

of SWCNT were determined to be 5.02 eV and 4.40 eV, respectively. Figure 19(b) shows Tauc plot: $(\alpha E_{ph})^2$ as a function of E_{ph} calculated from UV-vis-NIR absorption spectrum of SWCNT, where α is the absorption coefficient, and E_{ph} is photon energy. The optical bandgap of SWCNT, determined by the crossover point of the extrapolation line of Tauc plot and the x-axis, was determined to be 0.53 eV, which is smaller than the electrical bandgap (0.62 eV) determined by CV. Figure 19(c) and Figure 19(d) show the cut-off and onset regions of the UPS spectra of SWCNT, respectively. The Fermi level and HOMO level of SWCNT can be determined by the cut-off and onset regions, respectively, of the spectra with the following equations:

$$E_F = E_{BE_{max}} - h\nu$$

$$HOMO = h\nu - E_{BE_{max}} + E_{BE_{onset}}$$

where E_F is the Fermi level, $E_{BE_{max}}$ is the crossover point of the extrapolation of the spectra with x-axis, $E_{BE_{onset}}$ is the onset binding energy of the spectra, $h\nu$ is the energy of the incident photon. The Fermi level and HOMO from UPS were found to be 5.02 eV and 5.00 eV, respectively. Note that the HOMO level found from CV (5.02 eV) and UPS (5.00 eV) were fairly close. HOMO, LUMO, and Fermi level of DWCNT, MWCNT, and PEDOT were determined by the same methods. The CV curves for PEDOT:PSS and DWCNT are shown in Figure 20. The Tauc plot of DWCNT is shown in Figure 21. The UPS spectra of PEDOT, DWCNT and MWCNT are shown in Figure 22.

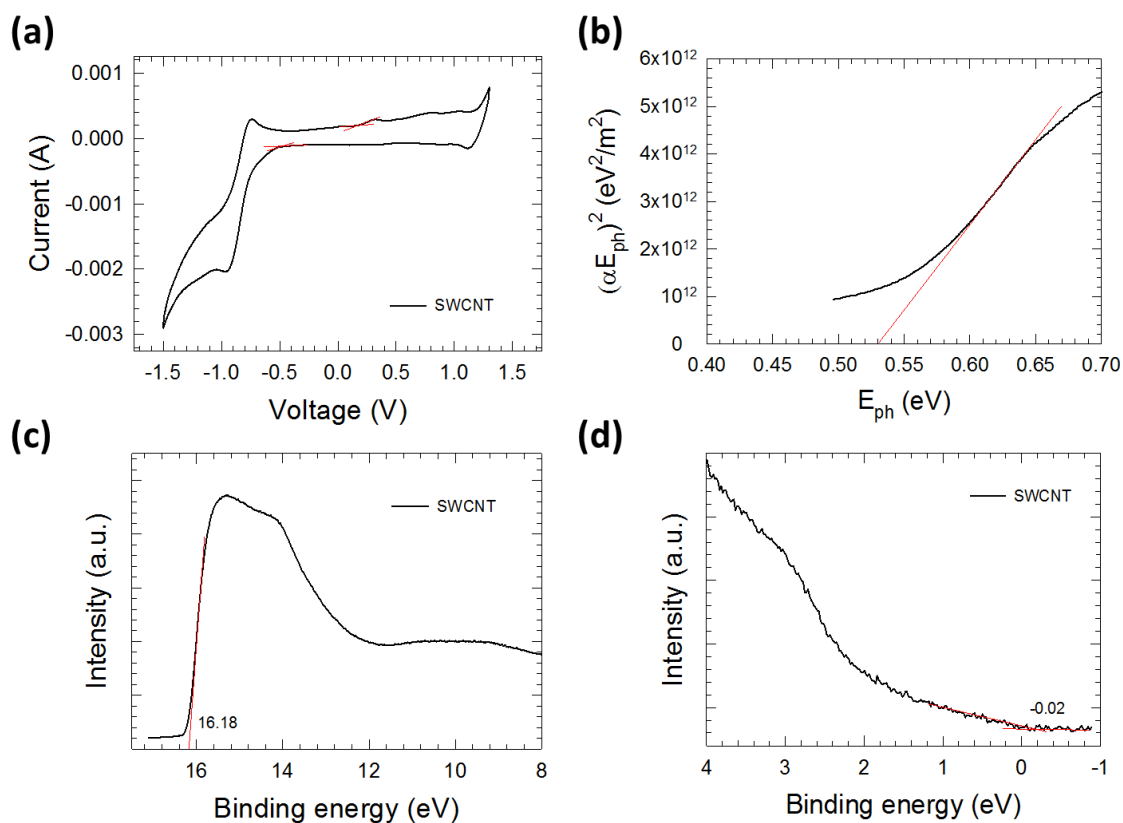


Figure 19. (a) CV curve of SWCNT. The red crosses show the onset potential of oxidation and reduction peaks. (b) Tauc plot: $(\alpha E_{ph})^2$ as a function of E_{ph} calculated from UV-vis-NIR absorption spectrum of SWCNT. The optical bandgap of SWCNT is determined by the extrapolation line to be 0.53 eV. (c) Cut-off and (d) onset region of the UPS spectra of SWCNT. The Fermi level and HOMO can be found to be 5.02 eV and 5.00 eV, respectively.

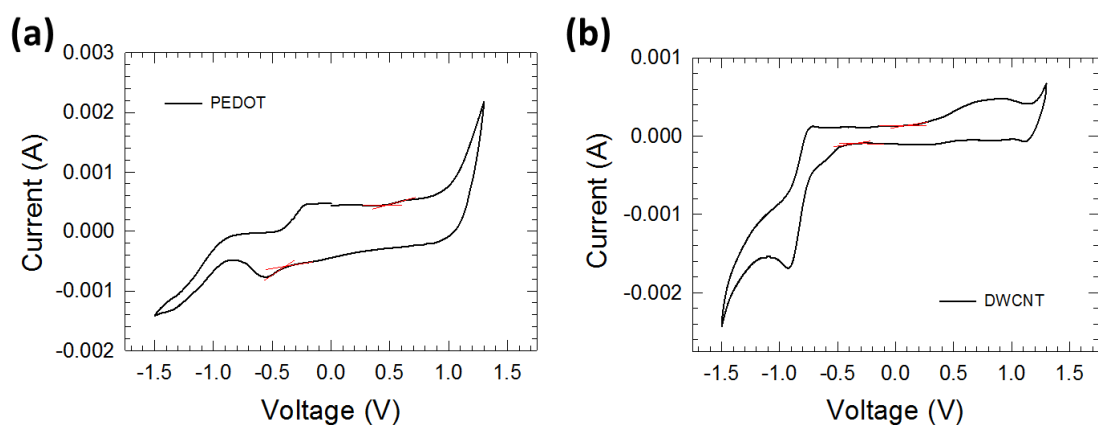


Figure 20. CV curve of PEDOT (a) and DWCNT (b). For PEDOT, HOMO and LUMO are determined to be 4.83 eV and 3.98 eV, respectively. For DWCNT, HOMO and LUMO are determined to be 4.89 eV and 4.51 eV, respectively.

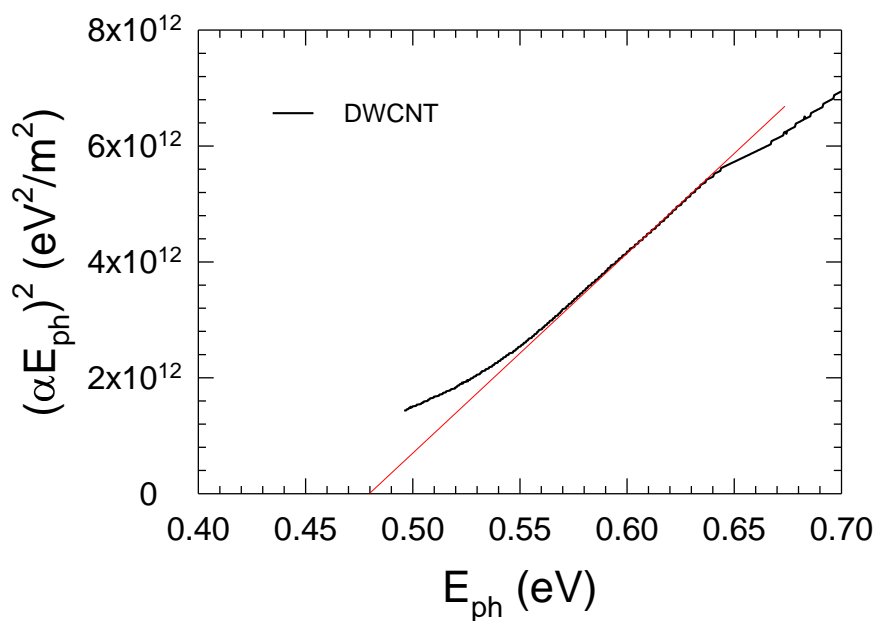


Figure 21. Tauc plot of DWCNT. The optical bandgap of DWCNT is determined by the extrapolation line to be 0.48 eV.

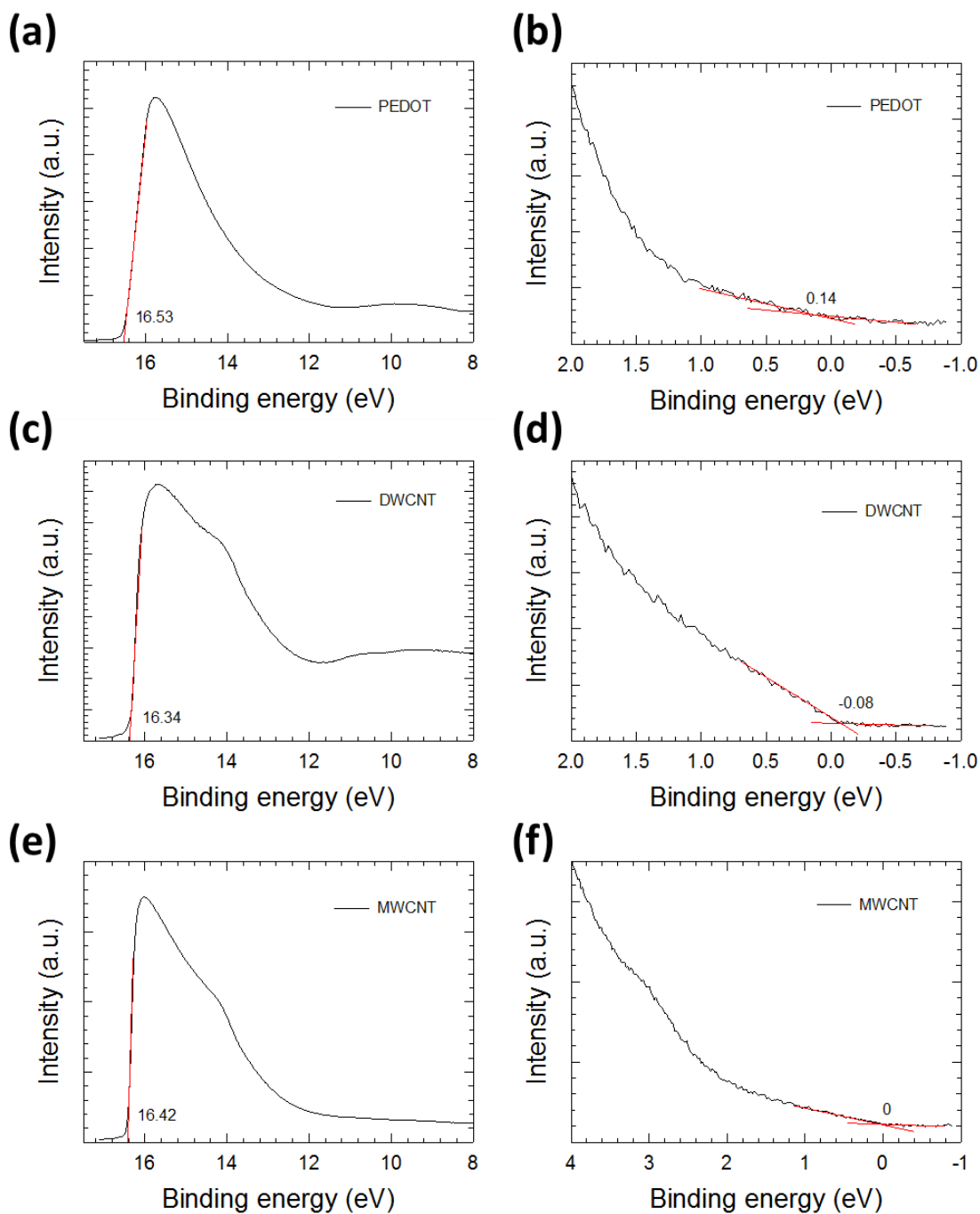


Figure 22. Cut-off and onset region of the UPS spectra of PEDOT ((a), (b)), DWCNT ((c), (d)), and MWCNT ((e), (f)). The Fermi level and HOMO of PEDOT are 4.67 eV and 4.81 eV, respectively. The Fermi level and HOMO of DWCNT are 4.67 eV and 4.81 eV, respectively. The Fermi level and HOMO of MWCNT are both 4.78 eV.

The measured bandgaps of SWCNT and DWCNT are summarized in Table 5 and compared with theoretical values calculated from the formula $E_{gap} = (4\hbar v_F/3d_{CNT})$. We can see that both electrical and optical bandgaps become smaller as the diameter of CNT increases.

Table 5. Electrical bandgap (obtained from CV), optical bandgap (obtained from UV-vis), and theoretical bandgap of SWCNT and DWCNT.

Material	Electrical bandgap (eV)	Optical bandgap (eV)	Theoretical bandgap (eV)
SWCNT	0.62	0.53	0.56
DWCNT	0.38	0.48	0.37

The Fermi level can also be determined by KPFM with gold foil as a reference and by the following equations:

$$WF_{tip} = WF_{Au} + CPD_{Au}$$

$$WF_{sample} = WF_{tip} - CPD_{sample}$$

where WF_{tip} , WF_{Au} , and WF_{sample} are work functions of the KPFM tip, gold reference, and sample, respectively. CPD_{Au} and CPD_{sample} are the contact potential differences between the tip and gold foil, and between the tip and the sample, respectively. Figure 23(a) shows the CPD profile of PEDOT, SWCNT, DWCNT, and MWCNT obtained from KPFM. Figure 23(b) shows the CPD profile of PEDOT as gate voltages of 0, 5,

10, 15, and 20 V were applied. It can be seen that the CPD of PEDOT was increased as larger gate voltage was applied. As a double check, Fermi levels obtained by KPFM were quite similar to that obtained by UPS.

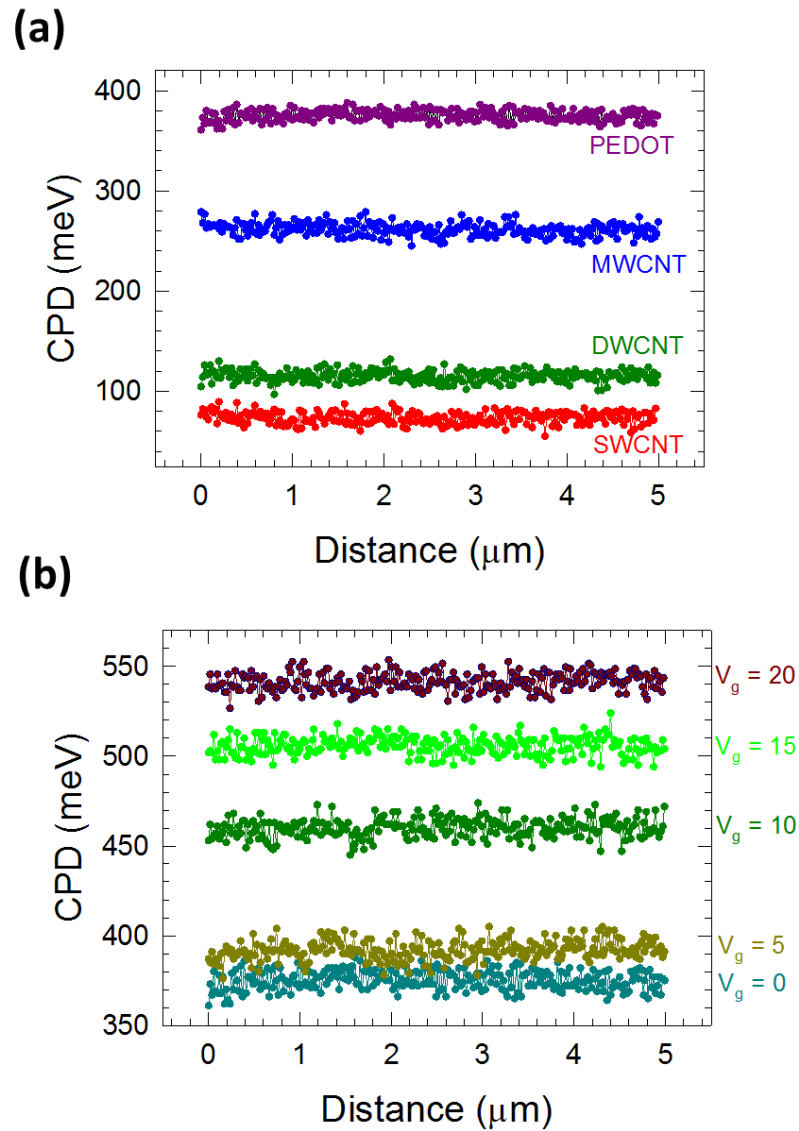


Figure 23. (a) CPD profile of PEDOT, SWCNT, DWCNT, and MWCNT obtained from KPFM. (b) CPD profile of PEDOT as gate voltages of 0, 5, 10, 15, and 20 V were applied.

Energy levels of PEDOT, SWCNT, DWCNT, MWCNT obtained from CV, UPS, and KPFM are summarized in Figure 24. It can be seen that from the HOMO and LUMO levels of CNTs, the electrical bandgap decreases with increased CNT diameter. This matches the trend predicted by the equation: $E_{gap} = 4\hbar V_F/3d_{CNT}$, where E_{gap} is the bandgap of CNT, \hbar is Planck constant, V_F is the Fermi velocity, d_{CNT} is the diameter of CNT. The electrical bandgap of SWCNT and DWCNT estimated by CV are 0.62 eV and 0.38 eV, respectively, which are close to the values (0.56 eV for SWCNT and 0.37 eV for DWCNT) predicted by the equation. Note that metallic MWCNT does not have bandgap. The Fermi level of SWCNT is very close to its HOMO. For DWCNT the Fermi level is larger than the HOMO level and is inside the band, showing that it is a degenerate semiconductor. This is one of the reasons that DWCNT film showed very high electrical conductivity as compared to other kinds of CNT films. The Fermi level obtained for PEDOT was inside the bandgap and was closer to its HOMO, showing that PEDOT used here is a p-type material with holes being the major charge carrier. Note that no matter what kind of CNT is under consideration, the work function of CNT is larger than the work function of PEDOT. Thus our previous assumption for the estimation of barrier height holds true. As positive gate voltage was applied to PEDOT, its Fermi level shifted upward, from 4.68 eV as $V_g = 0$ V to 4.52 eV as $V_g = 20$ V, showing that PEDOT is n-doped (but still a p-type material) and the carrier concentration was lowered.

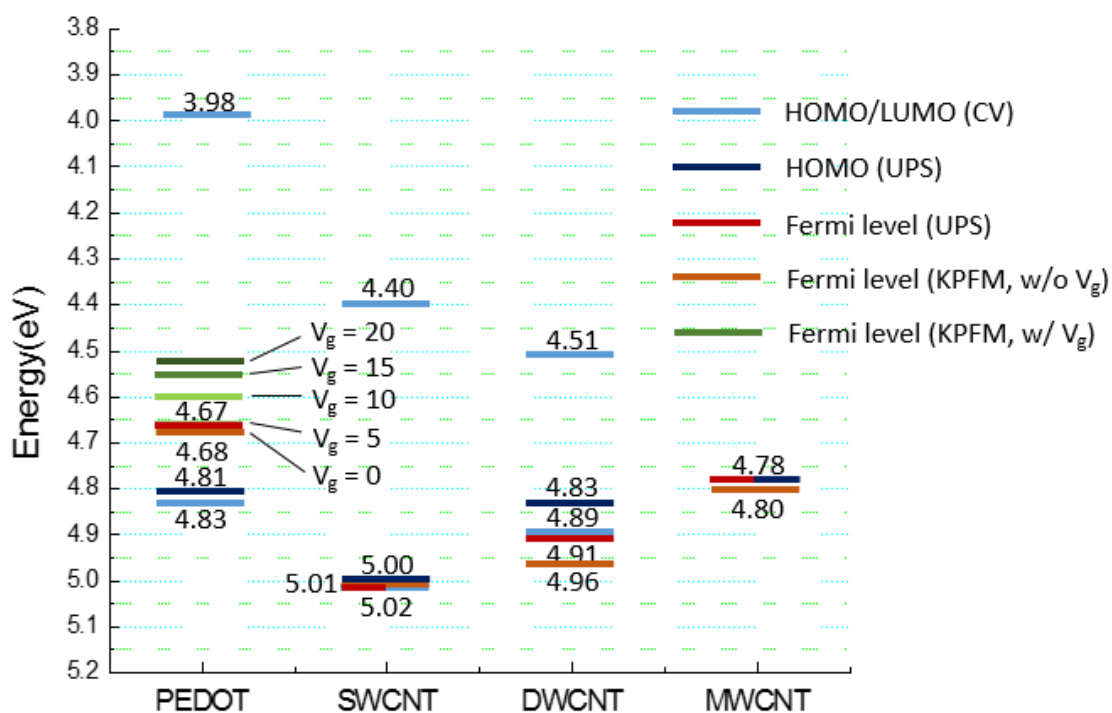


Figure 24. HOMO, LUMO, and Fermi levels of PEDOT, SWCNT, DWCNT, and MWCNT determined by CV, UPS, and KPDM. The Fermi levels of PEDOT measured as gate voltage of 0, 5, 10, 15, and 20 V were applied are also shown.

4.4.3 Barrier height analysis

With all the energy levels analyzed, we can now construct band diagrams for PEDOT-CNT junctions made with SWCNT, DWCNT, and MWCNT and estimate the barrier heights. Figure 25(a) shows the band diagram made of PEDOT-SWCNT junction as $V_g = 0$ V and $V_g = 20$ V. When $V_g = 0$ V, the barrier height for hole as the major carrier at the PEDOT-CNT junction was estimated to be 0.14 eV. Because of the barrier height, the thermopower and power factor of the junction device was superior to its component materials, CNT, and PEDOT. As V_g increased to 20 V, the barrier height increased to 0.3 eV. Thermopower was improved due to the increased barrier height. Similarly, the barrier height increased from 0.15 eV ($V_g = 0$ V) to 0.31 eV ($V_g = 20$ V) for double-wall and multi-wall CNT-PEDOT-CNT junctions (Figure 25(b),(c)). As a comparison, according to literatures, energy barriers leading to power factor improvement could range from 0.08 eV to 0.88 eV.[50-51]

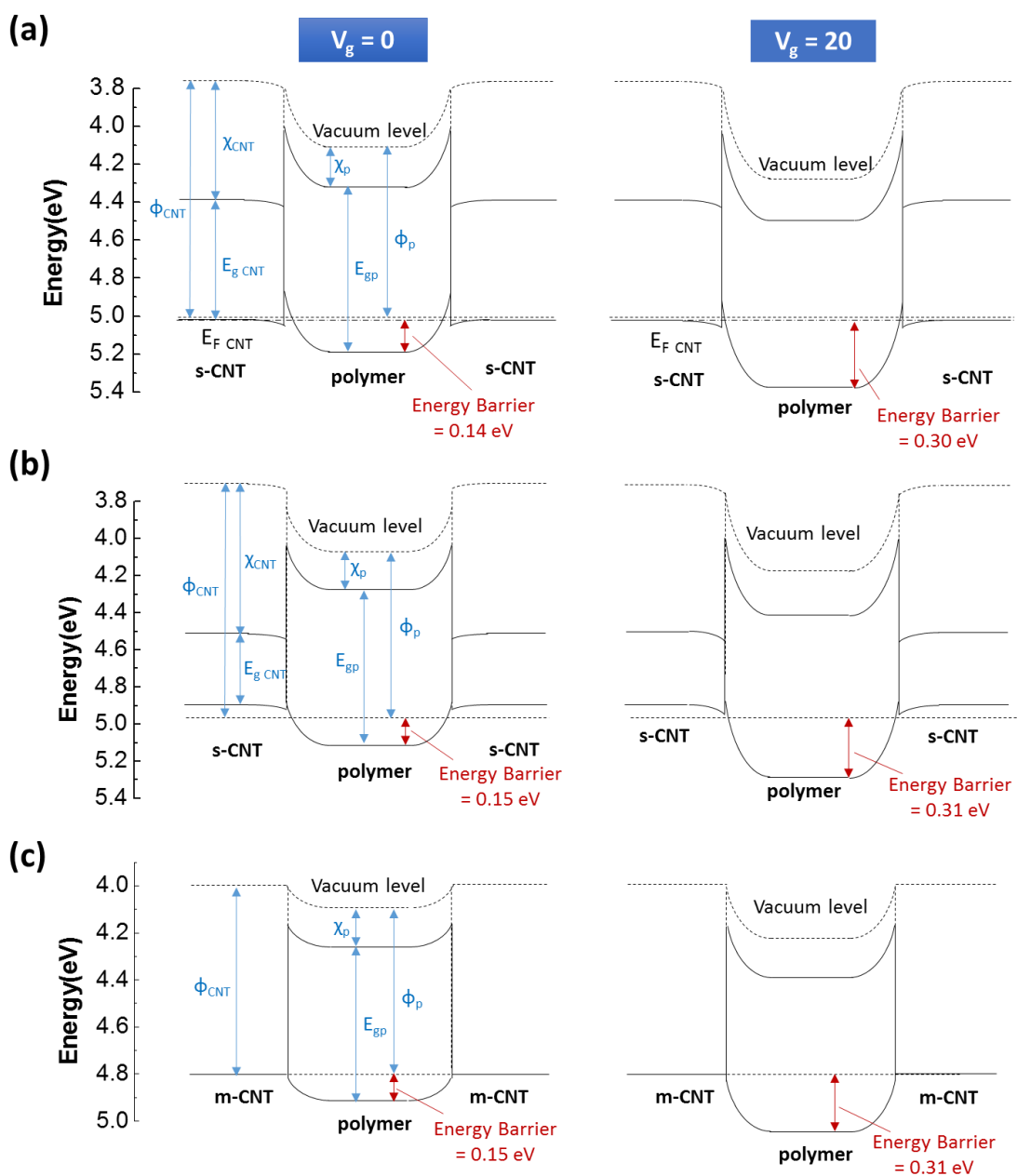


Figure 25. Band diagram of CNT-PEDOT-CNT junction made of SWCNT (a), DWCNT (b), and MWCNT (c) when no gate voltage (left) and gate voltage of 20 V are applied. Increase of barrier height for charge carrier can be seen as gate voltage is applied.

As discussed previously, change of PEDOT doping level and change of barrier height can both lead to thermopower improvement as gate voltage is applied. We tried to estimate the relative contribution of the two factors with the following analysis:

$$S_{total}(V_g) = S_{intrinsic}(V_g) + S_{barrier}(V_g)$$

where S_{total} is the thermopower as a function of gate voltage, $S_{intrinsic}$ is the thermopower of the junction device without the effect of energy filtering, and $S_{barrier}$ is the improvement of thermopower due to the effect of energy filtering. $S_{intrinsic}$ can be calculated by the sum of thermoelectric voltage generated by component materials (CNT and PEDOT) divided by total temperature difference across the junction:

$$S_{intrinsic}(V_g) = (S_{CNT}\Delta T_{CNT} + S_{polymer}(V_g)\Delta T_{polymer}) / \Delta T_{total}$$

where S_{CNT} is the intrinsic thermopower of CNT, ΔT_{CNT} is the temperature difference across CNT region, $S_{polymer}(V_g)$ is the thermopower of PEDOT as the function of gate voltage, and $\Delta T_{polymer}$ is the temperature difference across the PEDOT region. Figure 26 shows a schematic diagram of an OECT device bridged between hot side and cold side with ΔT_{CNT} and $\Delta T_{polymer}$ indicated.

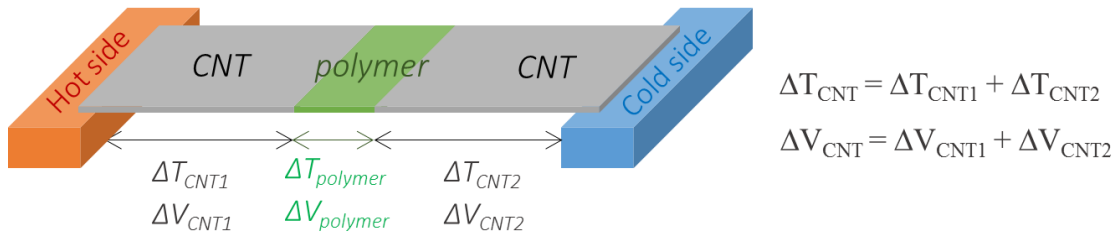


Figure 26. Schematic diagram showing an OECT device bridged between hot side and cold side. ΔT_{CNT} (the temperature difference across CNT region) and $\Delta T_{polymer}$ (the temperature difference across the PEDOT region) are indicated.

The intrinsic and gate voltage dependent thermoelectric properties of CNTs and PEDOT are measured and shown in Figure 27.

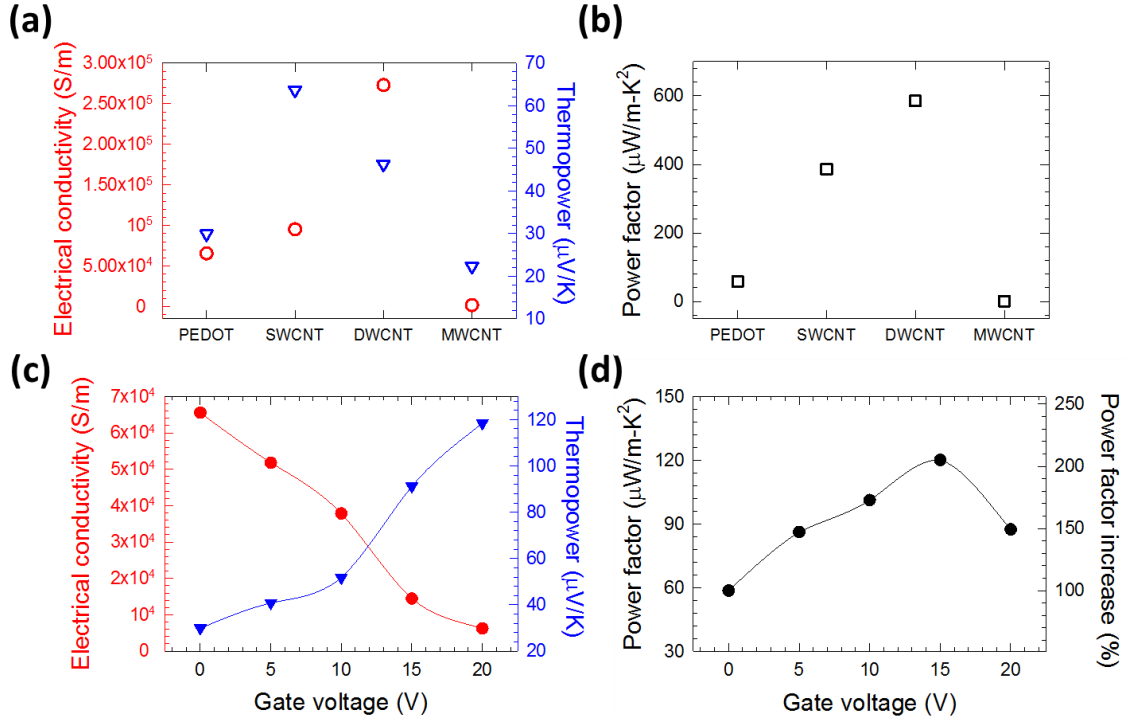


Figure 27. (a) Electrical conductivity, thermopower and (b) power factor of intrinsic PEDOT, SWCNT, DWCNT, and MWCNT. Gate voltage dependent thermoelectric properties of PEDOT are also shown in (c) and (d).

The improvement of thermopower due to the effect of energy filtering can be calculated as follows:

$$S_{barrier}(V_g) = S_{total}(V_g) - S_{intrinsic}(V_g) = S_{total}(V_g) - (S_{CNT}\Delta T_{CNT} + S_{polymer}(V_g)\Delta T_{polymer}) / \Delta T_{total}$$

The relative contribution of $S_{intrinsic}$ and $S_{barrier}$ is summarized in Figure 28. It can be seen that with increased gate voltage, the increase of $S_{intrinsic}$ is limited due to the

length of the PEDOT area is much shorter than that of the CNT area. It is clear that the improvement of overall thermopower majorly comes from the effect of energy barrier. Higher gate voltage leads to larger barrier at the junction, which filters out low energy barrier, leading to enhanced thermopower. Overall thermoelectric properties were optimized as a proper barrier height was present such that the negative effect of electrical conductivity reduction due to filtered out carrier was overcome by thermopower improvement.

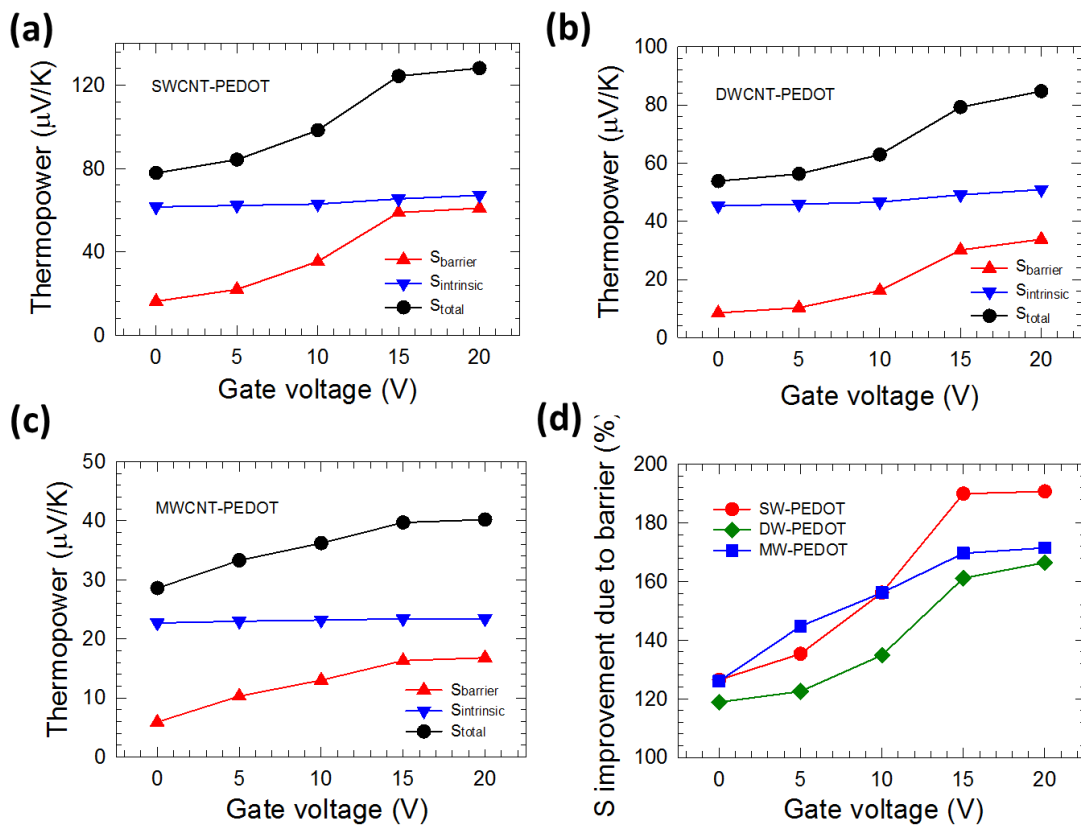


Figure 28. The relative contribution of thermopower from intrinsic property change and energy barrier filtering for devices made of SWCNT (a), DWCNT (b), and MWCNT (c). The percentages of thermopower improvement ($S_{\text{total}}/S_{\text{intrinsic}}$) due to energy filtering for devices made of different kinds of CNTs as a function of gate voltage are shown in (d).

4.4.4 PEDOT-CNT multi-junction device fabrication

In order to apply the obtained energy barrier height between PEDOT and CNT that lead to optimized thermoelectric properties to actual devices, we fabricated devices with multiple PEDOT-CNT junctions with controlled barrier height. We expect that with controlled barrier height, the thermopower would increase with number of junctions, leading to improved power factor. We firstly fabricated the devices with lift-off method: on photoresist coated CNT films we created multiple narrow gaps ($\sim 70 \mu\text{m}$ in width) by scratching the films with a razor blade. PEDOT:PSS film was then formed by spin coating on top of the sample to bridge the gaps. Subsequently, PEDOT film was lifted-off except for the part at the gap. The multi-junction devices were thus made. The PEDOT parts were reduced by hydrazine with the reduction time controlled such that the electrical conductivity of PEDOT is similar to that of PEDOT as $V_g = 15 \text{ V}$ in the OECT. The thermoelectric properties of devices made of lift-off method is shown in Figure 29. From the results we only see marginal thermopower improvement, presumably because of the large PEDOT width in the charge transport path.

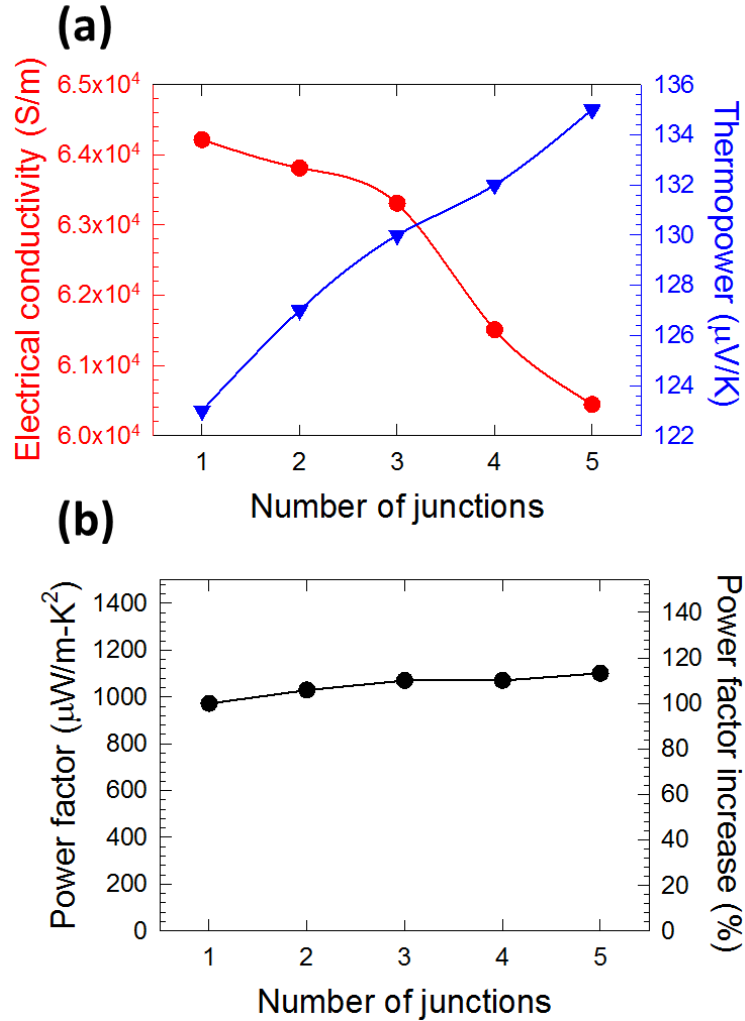


Figure 29. (a) Electrical conductivity and thermopower and (b) power factor of devices with 1 to 5 PEDOT-CNT junctions fabricated by lift-off method.

To reduce the transport path length of PEDOT, we further fabricated PEDOT-CNT multi-junction samples with layered method. CNT and PEDOT films were sprayed in sequence to overlap each other so that charges can transport from CNT film to a thin PEDOT film and then another CNT film, and so on. The PEDOT layers were controlled to be thin (55 nm). The thermoelectric properties of devices made of layered method is

shown in Figure 30. The trend that thermopower increased with the number of the junction was observed before it saturated at the junction number of 6. The reason for the increased trend of thermopower as the junction number is less than 6 is the tunneling of low energy charge carriers through the thin PEDOT film. As the junction number increased to be larger than 6, most of the tunneled charge carriers were filtered out, and the thermopower was maximized. On the other hand, electrical conductivity of the devices dropped as the number of junction increased due to the lower conductivity of PEDOT. The optimized power factor of up to $1299 \mu\text{W}/\text{m}\cdot\text{K}^2$ with the 6-junction sample, which is a decent value among organic thermoelectric materials.

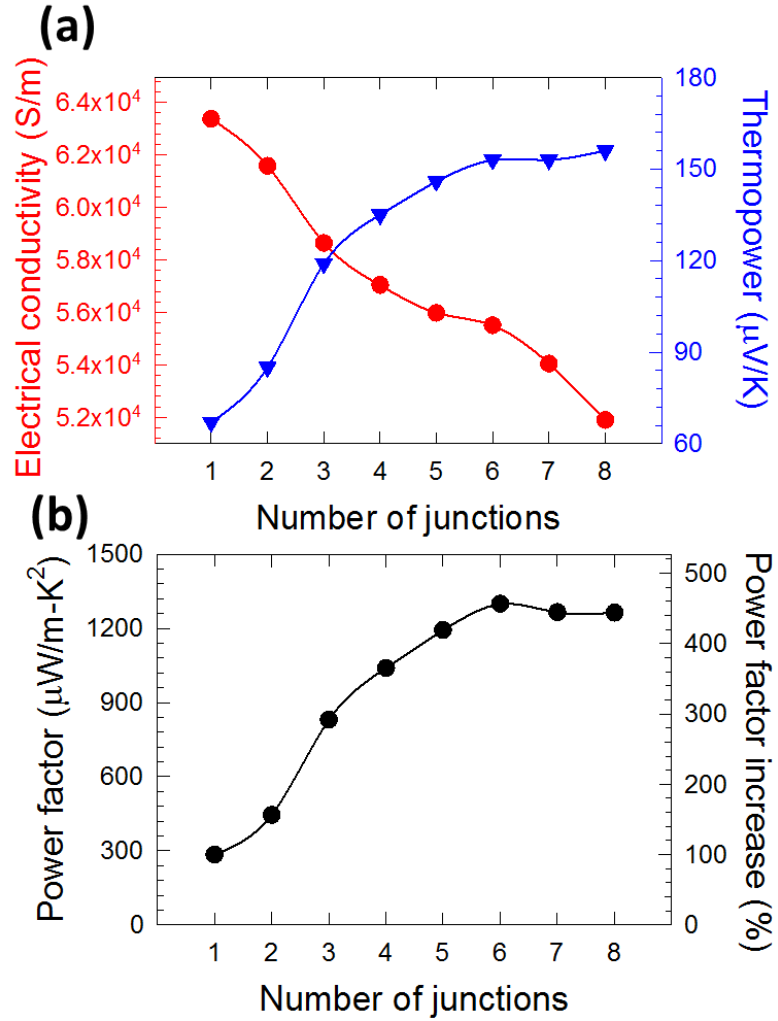


Figure 30. (a) Electrical conductivity and thermopower and (b) power factor of devices with 1 to 10 PEDOT-CNT junctions fabricated by layered method.

4.5 Conclusions

As a concluding remark, in this work energy filtering effect was, for the first time, demonstrated with quantitative barrier height analysis by electrochemical transistor. With our OECT, the Fermi level difference between CNT and PEDOT, and thus energy barrier height between them, can be readily adjustable by applying gate voltage. Power factor can be improved from $461 \mu\text{W}/\text{m}\cdot\text{K}^2$ to $1047 \mu\text{W}/\text{m}\cdot\text{K}^2$ as a gate voltage of 15 V was applied to the SWCNT device. To verify the effect of energy barrier on thermoelectric properties improvement, HOMO, LUMO, and Fermi level of CNT and PEDOT were obtained through CV, UV-vis, KPFM, and CV measurements. Energy band diagram at PEDOT-CNT junction was constructed with energy barrier height at different gate voltages estimated. The barrier height was 0.14 eV as $V_g = 0 \text{ V}$, 0.30 eV as $V_g = 20 \text{ V}$, and 0.27 eV as the power factor was optimized at $V_g = 15 \text{ V}$. The improvement of thermoelectric properties was mainly attributed to energy filtering effect at the junction instead of electrical property change due to the application of gate voltage, according to our calculation. We further apply the finding by fabricating devices with multiple PEDOT-CNT junctions with the barrier height between PEDOT and CNT adjusted to be 0.27 eV. A promising power factor of $1299 \mu\text{W}/\text{m}\cdot\text{K}^2$ was obtained. The power factor was found to be increase with the number of junctions before thermopower saturated at the junction number of 6. This study provides a pioneered investigation of energy filtering effect in organic thermoelectric materials and demonstrates an effective way for thermoelectric properties improvement.

CHAPTER V

SUMMARY

This dissertation aims to provide a better understanding of electronic and thermoelectric properties of organic thermoelectric composites. The ultimate goal is to suggest and demonstrate viable routes to thermoelectric performance improvement. To date, researches have been focused on fundamental understanding on conjugated polymers and carbon nanotubes and their respective physical and thermoelectric properties. However, the complicated interactions between them as they are made into composite are not clearly unveiled. These aspects, once clarified, could further boost up the efficiency of thermoelectric energy conversion.

In this dissertation, taking composites made of PEDOT:PSS and CNT as the system of study, I combined the strategies of hybridization and solvent treatment to form nanocomposites. As filler (CNTs) content and solvent treatment conditions were fine-tuned and optimized, the optimized power factor of 464 and 407 $\mu\text{W}/\text{m}\cdot\text{K}^2$ was obtained for DMSO and FA treated samples, respectively. Three intriguing behaviors exhibited by the composite are identified and further explored, including the origin of largely increased electrical conductivity and the unchanged thermopower after solvent/acid treatment, as well as the maximized thermopower at intermediate CNT concentration. Through compositional and morphological investigations, amount of filler inclusion and the effect of solvent treatment are correlated to electrical conductivity, carrier concentration, mobility, and thermopower in an attempt to elucidate the origin of the

aforementioned behaviors. Compositional and morphological study showed that the PSS removal and morphology change for the composites treated with polar solvents were suggested as important factors for the unusual electrical transport. The results indicate that the DMSO/FA treatment mainly removes insulating PSS, improving the carrier mobility and thereby electrical conductivity. However, this PSS removal did not noticeably change thermopower because thermopower is an intrinsic property that does not depend on volume. The energy filtering effect may play a role in maximizing thermopower at an intermediate level of CNT concentration because a moderate level of CNT percolation makes the PEDOT:PSS-CNT junction effect prominent. The highest power factor was observed at an intermediate CNT concentration, which can be mainly attributed to the unchanged or even increased thermopower despite large increase in electrical conductivity.

Identified as a crucial factor affecting thermoelectric behaviors of organic composites, the roles of material junctions and energy barrier are not sufficiently investigated by existing literatures, though. Here, experimental measurement of materials energetics is provided to quantitatively estimate barrier height. Also, the comparison of thermoelectric properties of a composite with that of pristine component materials is given to further clarify the effect of energy filtering. Organic electrochemical transistor was employed as a vehicle to tune energy barrier height at the junction and quantitatively correlate barrier height to electrical conductivity and thermopower. Band diagrams at the junction were constructed by measuring HOMO, LUMO, and Fermi levels determined by CV, KPFM, and UPS with and without

applying gate voltage. I observed an optimized power factor of $1047 \mu\text{W}/\text{m}\cdot\text{K}^2$ with a 15 V gate voltage and 0.27 eV energy barrier. The 2.3 times improvement of power factor compared to 0 gate voltage situation was mainly due to the enhancement of thermopower. From the calculation, thermopower improvement was majorly originated from the barrier effect. Actual multi-junction device fabrication showed the relation of thermopower with the number of junctions. Devices with multiple PEDOT-CNT junctions were fabricated with barrier height fine-tuned through hydrazine reduction to the optimized condition (0.27 eV). Thermopower increased with the number of junctions until it saturated at the junction number of 6. Correspondingly, a promising power factor of up to $1299 \mu\text{W}/\text{m}\cdot\text{K}^2$ was obtained. With a better understanding of charge carrier transport at the junction of thermoelectric materials, this study demonstrates a viable way for thermoelectric properties improvement.

REFERENCES

1. Snyder, G.J. and E.S. Toberer, *Complex thermoelectric materials*. Nature Materials, 2008. **7**: p. 105.
2. Zhao, L.-D., et al., *Ultra-high power factor and thermoelectric performance in hole-doped single-crystal SnSe*. Science, 2016. **351**(6269): p. 141-144.
3. Zhao, L.-D., et al., *Ultralow thermal conductivity and high thermoelectric figure of merit in SnSe crystals*. Nature, 2014. **508**(7496): p. 373-377.
4. Liu, W., et al., *New insight into the material parameter B to understand the enhanced thermoelectric performance of $Mg_2Sn_{1-x-y}Ge_xSb_y$* , Energ. Environ. Sci., 2016. **9**(2): p. 530-539.
5. Tang, Y., et al., *Convergence of multi-valley bands as the electronic origin of high thermoelectric performance in $CoSb_3$ skutterudites*. Nature Mat., 2015. **14**: p. 1223-1228
6. Kim, S.I., et al., *Dense dislocation arrays embedded in grain boundaries for high-performance bulk thermoelectrics*. Science, 2015. **348**(6230): p. 109-114.
7. Heremans, J.P., et al., *Enhancement of thermoelectric efficiency in $PbTe$ by distortion of the electronic density of states*. Science, 2008. **321**(5888): p. 554-557.
8. Heremans, J.P., B. Wiendlocha, and A.M. Chamoire, *Resonant levels in bulk thermoelectric semiconductors*. Energ. Environ. Sci., 2012. **5**(2): p. 5510-5530.

9. Pei, Y., et al., *Convergence of electronic bands for high performance bulk thermoelectrics*. Nature, 2011. **473**(7345): p. 66-69.
10. Vineis, C.J., et al., *Nanostructured thermoelectrics: big efficiency gains from small features*. Adv. Mater., 2010. **22**(36): p. 3970-3980.
11. Minnich, A., et al., *Bulk nanostructured thermoelectric materials: current research and future prospects*. Energ. Environ. Sci., 2009. **2**(5): p. 466-479.
12. Majumdar, A., *Thermoelectricity in semiconductor nanostructures*. Science, 2004. **303**(5659): p. 777-778.
13. Snyder, G.J. and E.S. Toberer, *Complex thermoelectric materials*. Nature Mat., 2008. **7**(2): p. 105-114.
14. Zebarjadi, M., et al., *Perspectives on thermoelectrics: from fundamentals to device applications*. Energy & Environmental Science, 2012. **5**(1): p. 5147-5162.
15. Wang, C., et al., *Semiconducting π -Conjugated Systems in Field-Effect Transistors: A Material Odyssey of Organic Electronics*. Chemical Reviews, 2012. **112**(4): p. 2208-2267.
16. Walzer, K., et al., *Highly Efficient Organic Devices Based on Electrically Doped Transport Layers*. Chemical Reviews, 2007. **107**(4): p. 1233-1271.
17. Bubnova, O., et al., *Optimization of the thermoelectric figure of merit in the conducting polymer poly(3,4-ethylenedioxythiophene)*. Nature Materials, 2011. **10**: p. 429.
18. Yu, C., et al., *Thermoelectric Behavior of Segregated-Network Polymer Nanocomposites*. Nano Letters, 2008. **8**(12): p. 4428-4432.

19. Yu, C., et al., *Air-stable fabric thermoelectric modules made of N- and P-type carbon nanotubes*. Energy & Environmental Science, 2012. **5**(11): p. 9481-9486.
20. Yu, C., et al., *Light-Weight Flexible Carbon Nanotube Based Organic Composites with Large Thermoelectric Power Factors*. ACS Nano, 2011. **5**(10): p. 7885-7892.
21. Kim, D., et al., *Improved Thermoelectric Behavior of Nanotube-Filled Polymer Composites with Poly(3,4-ethylenedioxythiophene) Poly(styrenesulfonate)*. ACS Nano, 2010. **4**(1): p. 513-523.
22. Cho, C., et al., *Completely Organic Multilayer Thin Film with Thermoelectric Power Factor Rivaling Inorganic Tellurides*. Advanced Materials, 2015. **27**(19): p. 2996-3001.
23. Russ, B., et al., *Power Factor Enhancement in Solution-Processed Organic n-Type Thermoelectrics Through Molecular Design*. Advanced Materials, 2014. **26**(21): p. 3473-3477.
24. Coates, N.E., et al., *Effect of Interfacial Properties on Polymer–Nanocrystal Thermoelectric Transport*. Advanced Materials, 2013. **25**(11): p. 1629-1633.
25. Yee, S.K., et al., *Thermoelectric power factor optimization in PEDOT:PSS tellurium nanowire hybrid composites*. Physical Chemistry Chemical Physics, 2013. **15**(11): p. 4024-4032.
26. Bubnova, O., M. Berggren, and X. Crispin, *Tuning the Thermoelectric Properties of Conducting Polymers in an Electrochemical Transistor*. Journal of the American Chemical Society, 2012. **134**(40): p. 16456-16459.

27. Xuan, Y., et al., *Thermoelectric properties of conducting polymers: The case of poly(3-hexylthiophene)*. Physical Review B, 2010. **82**(11): p. 115454.
28. Woo, C.H., et al., *A Quantitative Correlation between the Mobility and Crystallinity of Photo-Cross-Linkable P3HT*. Macromolecules, 2012. **45**(7): p. 3057-3062.
29. Steyrlleuthner, R., et al., *The Role of Regioregularity, Crystallinity, and Chain Orientation on Electron Transport in a High-Mobility n-Type Copolymer*. Journal of the American Chemical Society, 2014. **136**(11): p. 4245-4256.
30. Meng, X., et al., *Grain Boundary Engineering for Achieving High Thermoelectric Performance in n-Type Skutterudites*. Advanced Energy Materials, 2017. **7**(13): p. 1602582.
31. Sun, Y., et al., *A three-in-one improvement in thermoelectric properties of polyaniline brought by nanostructures*. Synthetic Metals, 2010. **160**(21): p. 2371-2376.
32. Taggart, D.K., et al., *Enhanced Thermoelectric Metrics in Ultra-long Electrodeposited PEDOT Nanowires*. Nano Letters, 2011. **11**(1): p. 125-131.
33. Qu, S., et al., *Highly anisotropic P3HT films with enhanced thermoelectric performance via organic small molecule epitaxy*. Npg Asia Materials, 2016. **8**: p. e292.
34. Friedel, B., et al., *Effects of Layer Thickness and Annealing of PEDOT:PSS Layers in Organic Photodetectors*. Macromolecules, 2009. **42**(17): p. 6741-6747.

35. Kim, G.H., et al., *Engineered doping of organic semiconductors for enhanced thermoelectric efficiency*. Nature Materials, 2013. **12**: p. 719.
36. Sootsman, J.R., et al., *Strong Reduction of Thermal Conductivity in Nanostructured PbTe Prepared by Matrix Encapsulation*. Chemistry of Materials, 2006. **18**(21): p. 4993-4995.
37. Chan Yu King, R., et al., *Carbon nanotube-polyaniline nanohybrids: Influence of the carbon nanotube characteristics on the morphological, spectroscopic, electrical and thermoelectric properties*. Synthetic Metals, 2012. **162**(15): p. 1348-1356.
38. Bubnova, O., et al., *Semi-metallic polymers*. Nature Materials, 2013. **13**: p. 190.
39. McGrail, B.T., A. Sehirlioglu, and E. Pentzer, *Polymer Composites for Thermoelectric Applications*. Angewandte Chemie International Edition, 2015. **54**(6): p. 1710-1723.
40. Hiroshige, Y., M. Ookawa, and N. Toshima, *Thermoelectric figure-of-merit of iodine-doped copolymer of phenylenevinylene with dialkoxyphenylenevinylene*. Synthetic Metals, 2007. **157**(10): p. 467-474.
41. Aïch, R.B., et al., *Electrical and Thermoelectric Properties of Poly(2,7-Carbazole) Derivatives*. Chemistry of Materials, 2009. **21**(4): p. 751-757.
42. Kemp, N.T., et al., *Thermoelectric power and conductivity of different types of polypyrrole*. Journal of Polymer Science Part B: Polymer Physics, 1999. **37**(9): p. 953-960.

43. Kaneko, H., et al., *Magnetoresistance and thermoelectric power studies of metal-nonmetal transition in iodine-doped polyacetylene*. Synthetic Metals, 1993. **57**(2): p. 4900-4905.
44. Wang, H., et al., *Facile charge carrier adjustment for improving thermopower of doped polyaniline*. Polymer, 2013. **54**(3): p. 1136-1140.
45. Wang, H., et al., *Thermally Driven Large N-Type Voltage Responses from Hybrids of Carbon Nanotubes and Poly(3,4-ethylenedioxythiophene) with Tetrakis(dimethylamino)ethylene*. Advanced Materials, 2015. **27**(43): p. 6855-6861.
46. Park, H., et al., *Enhanced thermoelectric properties of PEDOT:PSS nanofilms by a chemical dedoping process*. Journal of Materials Chemistry A, 2014. **2**(18): p. 6532-6539.
47. Culebras, M., C.M. Gomez, and A. Cantarero, *Enhanced thermoelectric performance of PEDOT with different counter-ions optimized by chemical reduction*. Journal of Materials Chemistry A, 2014. **2**(26): p. 10109-10115.
48. Ouyang, J., et al., *On the mechanism of conductivity enhancement in poly(3,4-ethylenedioxythiophene):poly(styrene sulfonate) film through solvent treatment*. Polymer, 2004. **45**(25): p. 8443-8450.
49. Alemu, D., et al., *Highly conductive PEDOT:PSS electrode by simple film treatment with methanol for ITO-free polymer solar cells*. Energy & Environmental Science, 2012. **5**(11): p. 9662-9671.

50. Park, T., et al., *Flexible PEDOT electrodes with large thermoelectric power factors to generate electricity by the touch of fingertips*. Energy & Environmental Science, 2013. **6**(3): p. 788-792.
51. Massonnet, N., et al., *Improvement of the Seebeck coefficient of PEDOT:PSS by chemical reduction combined with a novel method for its transfer using free-standing thin films*. Journal of Materials Chemistry C, 2014. **2**(7): p. 1278-1283.
52. Song, H., et al., *Fabrication of a layered nanostructure PEDOT:PSS/SWCNTs composite and its thermoelectric performance*. RSC Advances, 2013. **3**(44): p. 22065-22071.
53. Lee, W., et al., *Improving the thermoelectric power factor of CNT/PEDOT:PSS nanocomposite films by ethylene glycol treatment*. RSC Advances, 2016. **6**(58): p. 53339-53344.
54. Zhang, B., et al., *Promising Thermoelectric Properties of Commercial PEDOT:PSS Materials and Their Bi₂Te₃ Powder Composites*. ACS Applied Materials & Interfaces, 2010. **2**(11): p. 3170-3178.
55. Choi, K. and C. Yu, *Highly Doped Carbon Nanotubes with Gold Nanoparticles and Their Influence on Electrical Conductivity and Thermopower of Nanocomposites*. PLoS ONE, 2012. **7**(9): p. e44977.
56. See, K.C., et al., *Water-Processable Polymer–Nanocrystal Hybrids for Thermoelectrics*. Nano Letters, 2010. **10**(11): p. 4664-4667.
57. Avery, A.D., et al., *Tailored semiconducting carbon nanotube networks with enhanced thermoelectric properties*. Nature Energy, 2016. **1**: p. 16033.

58. Prasher, R.S., et al., *Turning Carbon Nanotubes from Exceptional Heat Conductors into Insulators*. Physical Review Letters, 2009. **102**(10): p. 105901.
59. Abad, B., et al., *Improved power factor of polyaniline nanocomposites with exfoliated graphene nanoplatelets (GNPs)*. Journal of Materials Chemistry A, 2013. **1**(35): p. 10450-10457.
60. Zhao, Y., et al., *The effect of graphite oxide on the thermoelectric properties of polyaniline*. Carbon, 2012. **50**(8): p. 3064-3073.
61. Kim, D., et al., *Improved thermoelectric behavior of nanotube-filled polymer composites with poly(3,4-ethylenedioxythiophene) poly(styrenesulfonate)*. ACS Nano, 2010. **4**: p. 513-523.
62. Yu, C., et al., *Light-weight flexible carbon nanotube based organic composites with large thermoelectric power factors*. ACS Nano, 2011. **5**: p. 7885-7892.
63. Terrones, M., *Science and Technology of the Twenty-First Century: Synthesis, Properties, and Applications of Carbon Nanotubes*. Annual Review of Materials Research, 2003. **33**(1): p. 419-501.
64. Blackburn, J.L., et al., *Carbon-Nanotube-Based Thermoelectric Materials and Devices*. Advanced Materials, 2018. p. 1704386.
65. Oh, D.H. and Y.H. Lee, *Stability and cap formation mechanism of single-walled carbon nanotubes*. Physical Review B, 1998. **58**(11): p. 7407-7411.
66. Zide, J.M.O., et al., *Demonstration of electron filtering to increase the Seebeck coefficient in $In_{0.53}Ga_{0.47}As/In_{0.53}Ga_{0.28}Al_{0.19}As$ superlattices*. Physical Review B, 2006. **74**(20): p. 205335.

67. Heremans, J.P., C.M. Thrush, and D.T. Morelli, *Thermopower enhancement in lead telluride nanostructures*. Physical Review B, 2004. **70**(11): p. 115334.
68. Heremans, J.P., C.M. Thrush, and D.T. Morelli, *Thermopower enhancement in PbTe with Pb precipitates*. Journal of Applied Physics, 2005. **98**(6): p. 063703.
69. Zhang, Y., et al., *Silver-Based Intermetallic Heterostructures in Sb₂Te₃ Thick Films with Enhanced Thermoelectric Power Factors*. Nano Letters, 2012. **12**(2): p. 1075-1080.
70. Meng, C., C. Liu, and S. Fan, *A Promising Approach to Enhanced Thermoelectric Properties Using Carbon Nanotube Networks*. Advanced Materials, 2010. **22**(4): p. 535-539.
71. Zhang, K., Y. Zhang, and S. Wang, *Enhancing thermoelectric properties of organic composites through hierarchical nanostructures*. Scientific Reports, 2013. **3**: p. 3448.
72. Wang, H., S.-i. Yi, and C. Yu, *Engineering electrical transport at the interface of conjugated carbon structures to improve thermoelectric properties of their composites*. Polymer, 2016. **97**: p. 487-495.
73. Choi, J., et al., *High-Performance Thermoelectric Paper Based on Double Carrier-Filtering Processes at Nanowire Heterojunctions*. Advanced Energy Materials, 2016. **6**(9): p. 1502181.

74. He, M., et al., *Thermopower enhancement in conducting polymer nanocomposites via carrier energy scattering at the organic-inorganic semiconductor interface*. Energy & Environmental Science, 2012. **5**(8): p. 8351-8358.
75. Lee, S.H., et al., *Novel solution-processable, dedoped semiconductors for application in thermoelectric devices*. Journal of Materials Chemistry A, 2014. **2**(33): p. 13380-13387.
76. Gasiorowski, J., et al., *Surface morphology, optical properties and conductivity changes of poly(3,4-ethylenedioxythiophene):poly(styrenesulfonate) by using additives*. Thin Solid Films, 2013. **536**: p. 211-215.
77. Mengistie, D.A., et al., *Highly Conductive PEDOT:PSS Treated with Formic Acid for ITO-Free Polymer Solar Cells*. ACS Applied Materials & Interfaces, 2014. **6**(4): p. 2292-2299.
78. Tsai, T.-C., et al., *A facile dedoping approach for effectively tuning thermoelectricity and acidity of PEDOT:PSS films*. Organic Electronics, 2014. **15**(3): p. 641-645.
79. Wang, H., et al., *Simultaneously Improving Electrical Conductivity and Thermopower of Polyaniline Composites by Utilizing Carbon Nanotubes as High Mobility Conduits*. ACS Applied Materials & Interfaces, 2015. **7**(18): p. 9589-9597.

80. Coleman, H.W. and W.G. Steele, *General Uncertainty Analysis: Planning an Experiment and Application in Validation*, in *Experimentation, Validation, and Uncertainty Analysis for Engineers*. 2009, John Wiley & Sons, Inc. p. 85-119.
81. Wang, Q., et al., *Enhanced thermoelectric properties of CNT/PANI composite nanofibers by highly orienting the arrangement of polymer chains*. *Journal of Materials Chemistry*, 2012. **22**(34): p. 17612-17618.
82. Snyder, G.J. and E.S. Toberer, *Complex thermoelectric materials*. *Nat Mater*, 2008. **7**(2): p. 105-114.
83. Tazebay, A.S., et al., *Thermal Transport Driven by Extraneous Nanoparticles and Phase Segregation in Nanostructured Mg₂(Si,Sn) and Estimation of Optimum Thermoelectric Performance*. *ACS Appl. Mater. Interfaces*, 2016. **8**(11): p. 7003-7012.
84. Wei, Q., et al., *Recent Progress on PEDOT-Based Thermoelectric Materials*. *Materials*, 2015. **8**(2): p. 732.
85. Culebras, M., C. Gómez, and A. Cantarero, *Review on Polymers for Thermoelectric Applications*. *Materials*, 2014. **7**(9): p. 6701.
86. Qingshuo, W., et al., *Thermoelectric power enhancement of PEDOT:PSS in high-humidity conditions*. *Applied Physics Express*, 2014. **7**(3): p. 031601.
87. Bubnova, O., et al., *Semi-metallic polymers*. *Nat Mater*, 2014. **13**(2): p. 190-194.
88. Kim, G.H., et al., *Engineered doping of organic semiconductors for enhanced thermoelectric efficiency*. *Nat Mater*, 2013. **12**(8): p. 719-723.

89. Moriarty, G.P., et al., *Fully Organic Nanocomposites with High Thermoelectric Power Factors by using a Dual-Stabilizer Preparation*. Energy Technology, 2013. **1**(4): p. 265-272.
90. Lee, S.H., et al., *Transparent and flexible organic semiconductor nanofilms with enhanced thermoelectric efficiency*. Journal of Materials Chemistry A, 2014. **2**(20): p. 7288-7294.
91. Jönsson, S.K.M., et al., *The effects of solvents on the morphology and sheet resistance in poly(3,4-ethylenedioxythiophene)–polystyrenesulfonic acid (PEDOT–PSS) films*. Synthetic Metals, 2003. **139**(1): p. 1-10.
92. Lang, U., et al., *Microscopical Investigations of PEDOT:PSS Thin Films*. Advanced Functional Materials, 2009. **19**(8): p. 1215-1220.
93. Crispin, X., et al., *The Origin of the High Conductivity of Poly(3,4-ethylenedioxythiophene)–Poly(styrenesulfonate) (PEDOT–PSS) Plastic Electrodes*. Chemistry of Materials, 2006. **18**(18): p. 4354-4360.
94. Unsworth, N.K., et al., *Comparison of dimethyl sulfoxide treated highly conductive poly(3,4-ethylenedioxythiophene):poly(styrenesulfonate) electrodes for use in indium tin oxide-free organic electronic photovoltaic devices*. Organic Electronics, 2014. **15**(10): p. 2624-2631.
95. Wei, Q., et al., *Morphological Change and Mobility Enhancement in PEDOT:PSS by Adding Co-solvents*. Advanced Materials, 2013. **25**(20): p. 2831-2836.

96. Choudhury, P.K., et al., *Modified conformation and physical properties in conducting polymers due to varying conjugation and solvent interactions*. Journal of Materials Chemistry, 2011. **21**(5): p. 1607-1614.
97. Ryu, Y., D. Freeman, and C. Yu, *High electrical conductivity and n-type thermopower from double-/single-wall carbon nanotubes by manipulating charge interactions between nanotubes and organic/inorganic nanomaterials*. Carbon, 2011. **49**(14): p. 4745-4751.
98. Dürkop, T., et al., *Extraordinary Mobility in Semiconducting Carbon Nanotubes*. Nano Letters, 2004. **4**(1): p. 35-39.
99. Kim, S.L., et al., *Flexible Power Fabrics Made of Carbon Nanotubes for Harvesting Thermoelectricity*. ACS Nano, 2014. **8**(3): p. 2377-2386.
100. Yi, S.-i. and C. Yu, *Modeling of thermoelectric properties of SiGe alloy nanowires and estimation of the best design parameters for high figure-of-merits*. Journal of Applied Physics, 2015. **117**(3): p. 035105.
101. Moriarty, G.P., et al., *Thermoelectric behavior of organic thin film nanocomposites*. Journal of Polymer Science Part B: Polymer Physics, 2013. **51**(2): p. 119-123.
102. Dörfling, B., et al., *Photoinduced p- to n-type Switching in Thermoelectric Polymer-Carbon Nanotube Composites*. Advanced Materials, 2016. **28**(14): p. 2782-2789.

103. Yu, C., et al., *Modulating Electronic Transport Properties of Carbon Nanotubes To Improve the Thermoelectric Power Factor via Nanoparticle Decoration*. ACS Nano, 2011. **5**(2): p. 1297-1303.
104. Scheele, M., et al., *Thermoelectric Properties of Lead Chalcogenide Core–Shell Nanostructures*. ACS Nano, 2011. **5**(11): p. 8541-8551.
105. Faleev, S.V. and F. Léonard, *Theory of enhancement of thermoelectric properties of materials with nano-inclusions*. Physical Review B, 2008. **77**(21): p. 214304.
106. Paul, B., A.K. V, and P. Banerji, *Embedded Ag-rich nanodots in PbTe: Enhancement of thermoelectric properties through energy filtering of the carriers*. Journal of Applied Physics, 2010. **108**(6): p. 064322.
107. Yu, C., et al., *Thermal Conductance and Thermopower of an Individual Single-Wall Carbon Nanotube*. Nano Letters, 2005. **5**(9): p. 1842-1846.
108. Ryu, Y., L. Yin, and C. Yu, *Dramatic electrical conductivity improvement of carbon nanotube networks by simultaneous de-bundling and hole-doping with chlorosulfonic acid*. Journal of Materials Chemistry, 2012. **22**(14): p. 6959-6964.
109. Minnich, A.J., et al., *Bulk nanostructured thermoelectric materials: current research and future prospects*. Energy & Environmental Science, 2009. **2**(5): p. 466-479.
110. Hasoon, S. and A. Ibrahim Abbo, *Optical and Electrical Properties of Thin Films of Polyaniline and Polypyrrole*. Vol. 7. 2012. 10666-10678.

111. Kanakamedala, S.K., et al., *A simple polymer based electrochemical transistor for micromolar glucose sensing*. *Sensors and Actuators B: Chemical*, 2011. **157**(1): p. 92-97.
112. Robinson, N.D., et al., *On the Current Saturation Observed in Electrochemical Polymer Transistors*. *Journal of The Electrochemical Society*, 2006. **153**(3): p. H39-H44.